

1 Seismo-acoustic and GNSS observations of a record-breaking Black 2 Sea storm: repurposing geophysical sensors for environmental 3 monitoring 4

5 Laura Petrescu^{1,2,*}, Bogdan Antonescu^{1,2}, Sorin Nistor³, Iustin Floroiu^{4,5}, Dragoş Ene¹, Daniela
6 Ghica¹, Constantin Ionescu¹, Andrei Anghel⁴, Mihai Datcu⁴
7

- 8 1. National Institute for Earth Physics, Magurele, Romania
- 9 2. University of Bucharest, Faculty of Physics, Magurele, Romania
- 10 3. University of Oradea, Faculty of Construction, Cadaster and Architecture, Oradea,
11 Romania
- 12 4. Politehnica University of Bucharest, Faculty of Electronics, Telecommunications and
13 Information Technology, Bucharest, Romania
- 14 5. Politehnica University of Bucharest, Doctoral School of Electronics,
15 Telecommunications & Information Technology, Bucharest, Romania

16
17 * laura.petrescu@infp.ro
18

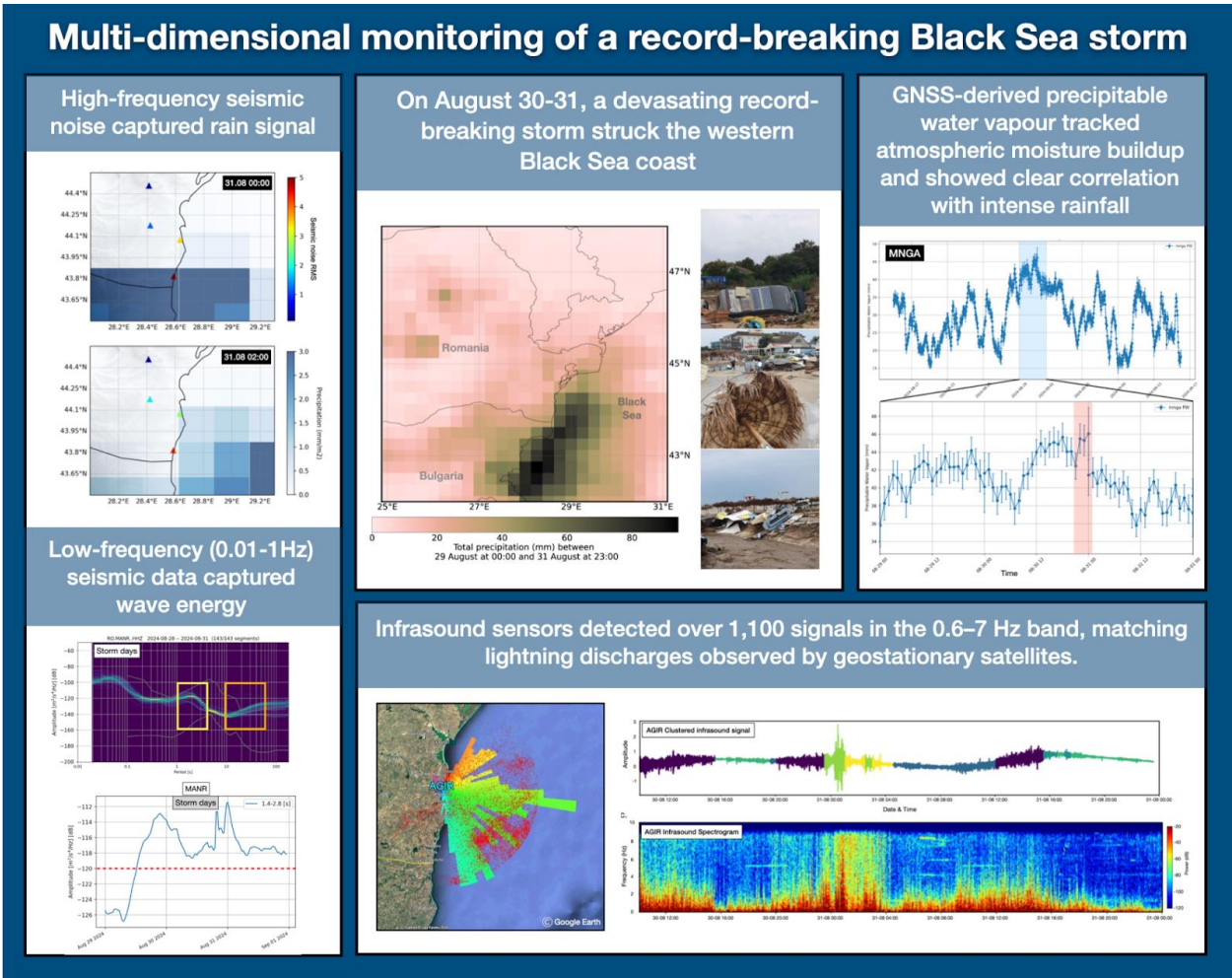
19 Abstract 20

21 In August 2024, a devastating storm struck Romania’s Black Sea coast, setting new precipitation
22 records and marking an unusual change relative to historical climate observations. To investigate
23 this extraordinary event, we integrated non-conventional sensors (seismic, GNSS, infrasound, and
24 satellite data) with ERA5 meteorological reanalysis to monitor storm dynamics. High-frequency
25 (>30 Hz) seismic signals captured precipitation, while microseismic bands (0.1-1Hz) reflected
26 wave-induced ground motion. Analysis of infrasound data via unsupervised learning delineated
27 periods of acoustic quiescence from storm-related activity. The temporal evolution of these
28 infrasound states coincided with distinct patterns in seismic ground motion, suggesting a shared
29 origin in the storm's atmospheric dynamics. The infrasound array also detected over 1,100 signals
30 in the 0.6-7 Hz band, matching lightning discharges observed by geostationary satellites. GNSS
31 data recorded a buildup of precipitable water vapor that peaked concurrently with intense rainfall,
32 following a multi-day increase that preceded the main storm phase. This study highlights the value
33 of integrating diverse, non-traditional datasets to enhance the resolution and depth of storm
34 analysis. Their combined use offers a more holistic understanding of storm evolution and supports
35 future research on the potential role of multi-sensor observations in improving early-warning
36 systems in vulnerable coastal regions.

37

38 **Graphical abstract**

39



40

41

42

43

44

45

46

47

48 **1. Introduction**

49 Climate change has become a critical global issue, with far-reaching effects on weather patterns
50 and the frequency and intensity of extreme events (Stott, 2016). These changes are not only
51 contributing to more severe weather events but also altering the timing, location, and duration of
52 storms, making them harder to predict and manage (Bengtsson et al., 2006). Understanding how
53 to effectively monitor and predict the behavior of storms, particularly extreme ones, is crucial for
54 improving forecasting models, enhancing early warning systems, and mitigating their impacts on
55 both natural and human systems.

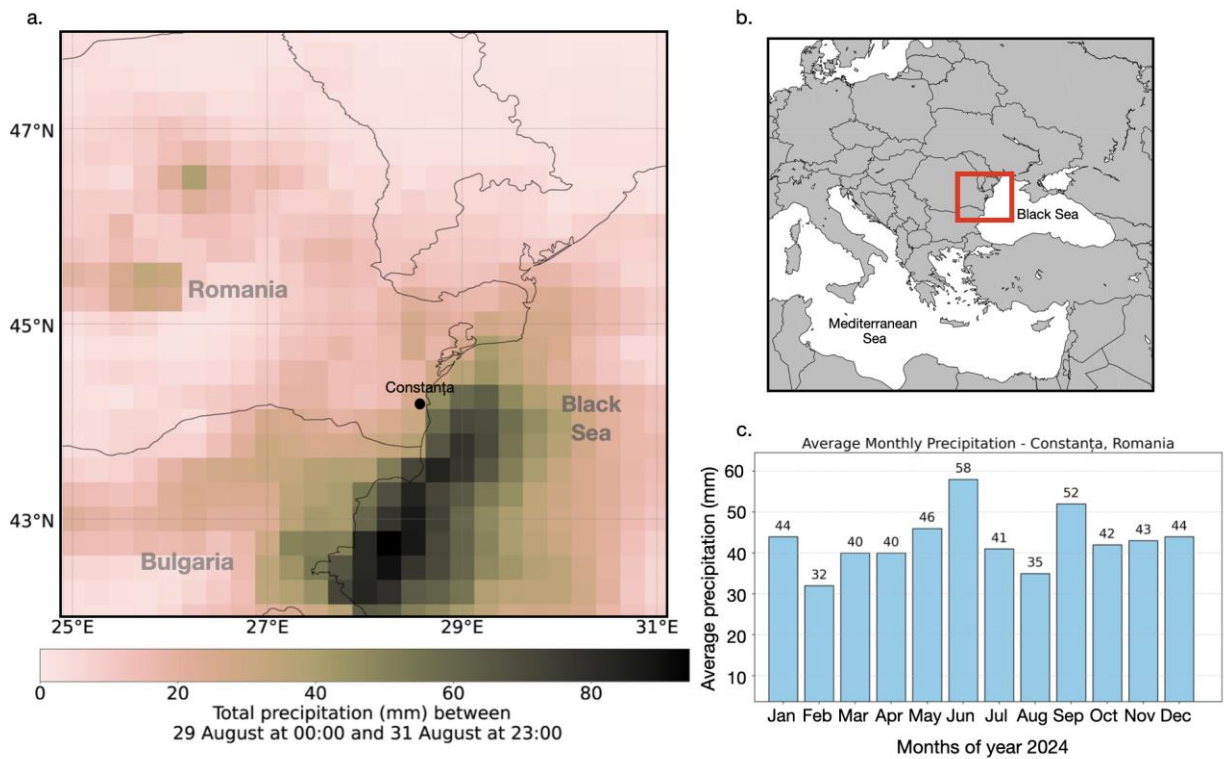
56 Traditional meteorological monitoring relies heavily on ground-based stations, weather radars, and
57 satellite observations to track and predict storm behavior (Kober and Tafferner, 2009). These
58 systems have been the backbone of weather forecasting for decades, providing valuable data on
59 temperature, pressure, wind speed, and precipitation. However, while these methods are effective,
60 they often have limitations in terms of spatial coverage (e.g. Sokol et al., 2021), particularly in
61 remote or hard-to-reach areas. Additionally, they may struggle to capture certain atmospheric
62 phenomena in real-time. As a result, non-conventional monitoring methods are increasingly being
63 integrated into storm tracking efforts to complement existing meteorological approaches (e.g. Bosity
64 et al., 2012; Burtin et al., 2016; Diaz et al., 2023; Coviello et al., 2024).

65 In this context, our study focuses on the integration of alternative environmental datasets, including
66 GNSS stations, infrasound sensors, and seismic data, to track the dynamics of an extreme storm
67 event, as part of a national climate change resilience strategy, implemented through the DTE
68 Climate project (<https://dteclimate.upb.ro/>). GNSS data provide valuable information on
69 atmospheric water vapor, helping to track moisture changes that influence storm formation and
70 intensity (Bosity et al, 2012; Marut et al., 2022). Infrasound sensors detect low-frequency acoustic
71 waves generated by storm activity, such as lightning or large-scale weather system movements
72 like microbaroms (e.g. Landès et al., 2012). Seismic data, though traditionally used for earthquake
73 monitoring, can also record vibrations caused by storm-induced pressure changes, making it useful
74 for detecting rainstorms, floods, or tropical cyclones (e.g. Retailleau and Gualtieri, 2021). Through
75 the integration of these diverse sensor networks, our work highlights their synergy in improving
76 storm detection, monitoring capabilities, and, potentially, early warning systems, contributing to
77 more robust climate resilience strategies.

78 **2. Study area and storm overview**

79
80 The Black Sea region (Figure 1) is characterized by a unique combination of geographic and
81 meteorological features that significantly influence its climate and weather patterns. Nestled
82 between Europe and Asia, the Black Sea is bordered by six countries with diverse landscapes, from
83 mountainous areas to flat plains. This geography, combined with the Black Sea's relatively shallow
84 waters compared to oceanic environments and its connection to the Mediterranean through the
85 Bosphorus Strait, creates an environment where rapid changes in weather are common.
86 Understanding the dynamics of these extreme weather events is crucial, as they can have a
87 profound impact on the environment, economy, and daily life in the region. Monitoring such events
88 is key to improving our ability to predict their occurrence and intensity. By studying the complex
89 atmospheric processes that govern these storms, we can enhance predictive models and refine early

90 warning systems, ultimately helping to mitigate the risks and protect the communities and
91 ecosystems most vulnerable to these extreme weather phenomena.



92
93 *Figure 1. a. Total precipitation accumulated (in mm, shaded according to the scale) between 29*
94 *August 00 UTC and 31 August 23:00 UTC extracted from ERA5 data. b. Map of Europe with red*
95 *square marking the study region; c. Average monthly precipitation rates in Constanța, Romania.*

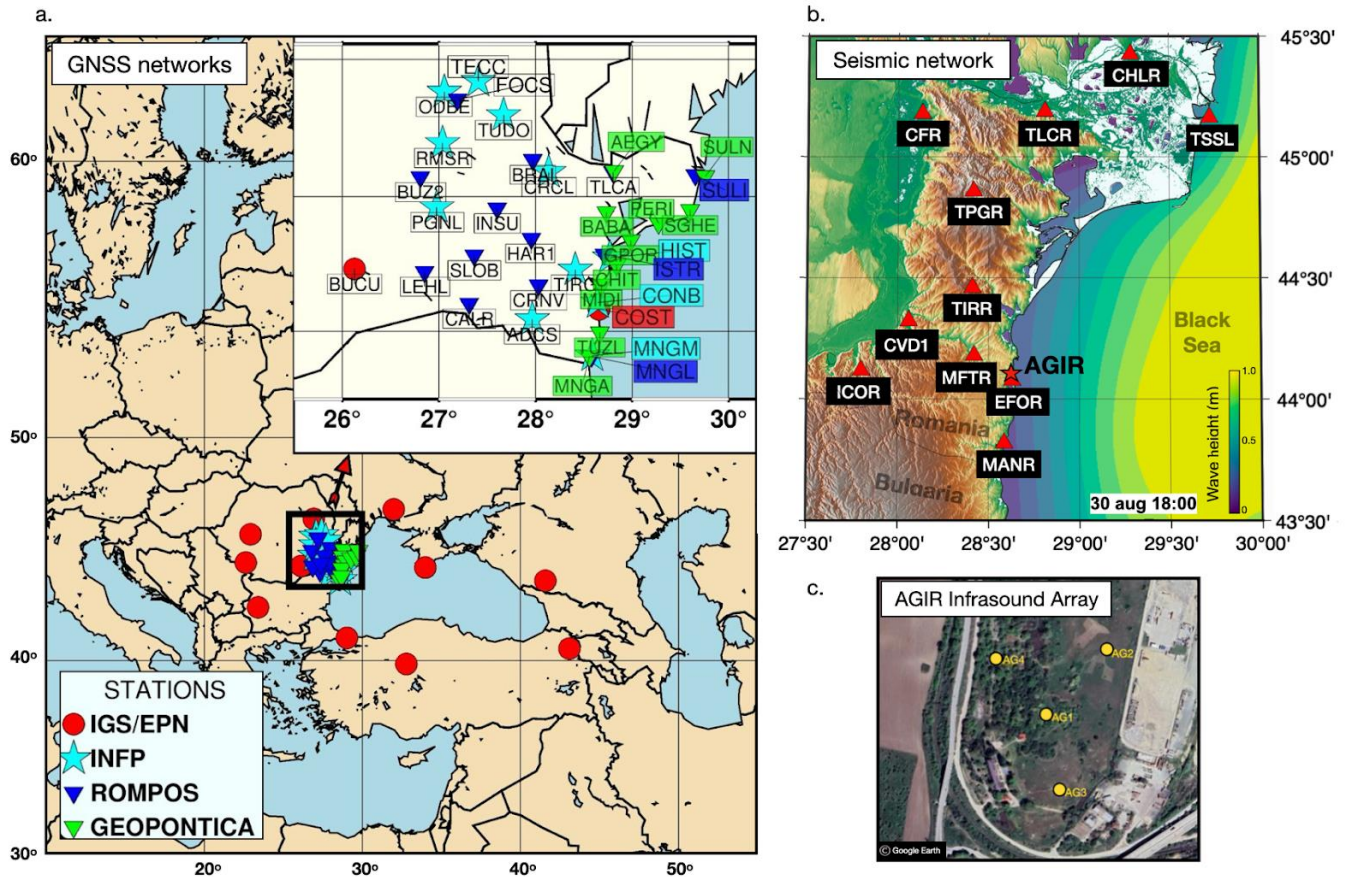
96 In August 2024, Romania experienced severe flooding, largely driven by a storm that brought
97 unusual precipitation patterns to the Black Sea coastal region. Exceptional precipitation totals were
98 recorded over south-eastern Romania in particular in Mangalia (234.7 mm), Agigea (145 mm),
99 and Tuzla (118 mm), leading to significant flooding in coastal towns (Figure 1). Over 800
100 emergency calls prompted large-scale intervention by ISU Dobrogea, focusing on evacuations,
101 debris clearance, and infrastructure restoration (Antonescu et al. 2024). According to the National
102 Meteorological Agency official records (https://www.meteoromania.ro/clim/caracterizare-lunara/cc_2024_08.html), one of the coastal stations at Mangalia, recorded a total of 343.6 mm of
103 precipitation in August 2024, breaking the previous record of 159.1 mm from 1947, and
104 significantly surpassing the average monthly precipitation values for this area (Figure 1c). A
105 remarkable 234.7 mm of this total fell in a single day on August 31, 2024, highlighting the event's
106 exceptional intensity.
107

108 An analysis by ClimaMeter (www.climameter.org, Faranda et al. 2024, Antonescu et al. 2024)
109 immediately after the storm, showed that low pressure systems similar to the one that caused the
110 floods typically produce 15% less rainfall in eastern Romania compared to historical trends.
111 However, this particular storm led to a significant local increase in precipitation, particularly in
112 Constanța, where daily rainfall reached up to 5 mm day⁻¹, or up to 10% more than usual.

113 ClimaMeter’s analysis compares events of this type to historical analogues over the past several
114 decades, providing context for how unusual this storm was. According to Antonescu et al. (2024),
115 the local precipitation anomaly in this event is mostly linked to human-induced climate change,
116 with natural climate variability playing a modest role. Studying this unusual storm and its
117 atmospheric characteristics demonstrates the value of using all available observational
118 infrastructure, including geophysical sensors, to monitor extreme precipitation events, gain
119 insights into atmospheric processes, and support preparedness and resilience in the context of
120 ongoing climate variability.

121 **3. Data and Methods**

122 The analysis of the storm event integrates a variety of data sources and methodologies to provide
123 a comprehensive understanding of its dynamics. Seismic data, infrasound measurements, GNSS
124 water vapor data, and ERA5 reanalysis data are all utilized to capture different aspects of the
125 storm’s behavior (Figure 2). Seismic data offers insights into ground vibrations and atmospheric
126 disturbances, while infrasound monitoring detects low-frequency acoustic signals generated by
127 lightning and other meteorological phenomena. GNSS water vapor data provides valuable
128 information on atmospheric moisture. Additionally, ERA5 reanalysis data (Hersbach et al. 2020),
129 which provides detailed atmospheric and wave dynamics data, helps contextualize the storm's
130 impact within broader weather patterns. Together, these diverse data sources enable a multifaceted
131 approach to studying the storm and its effects.



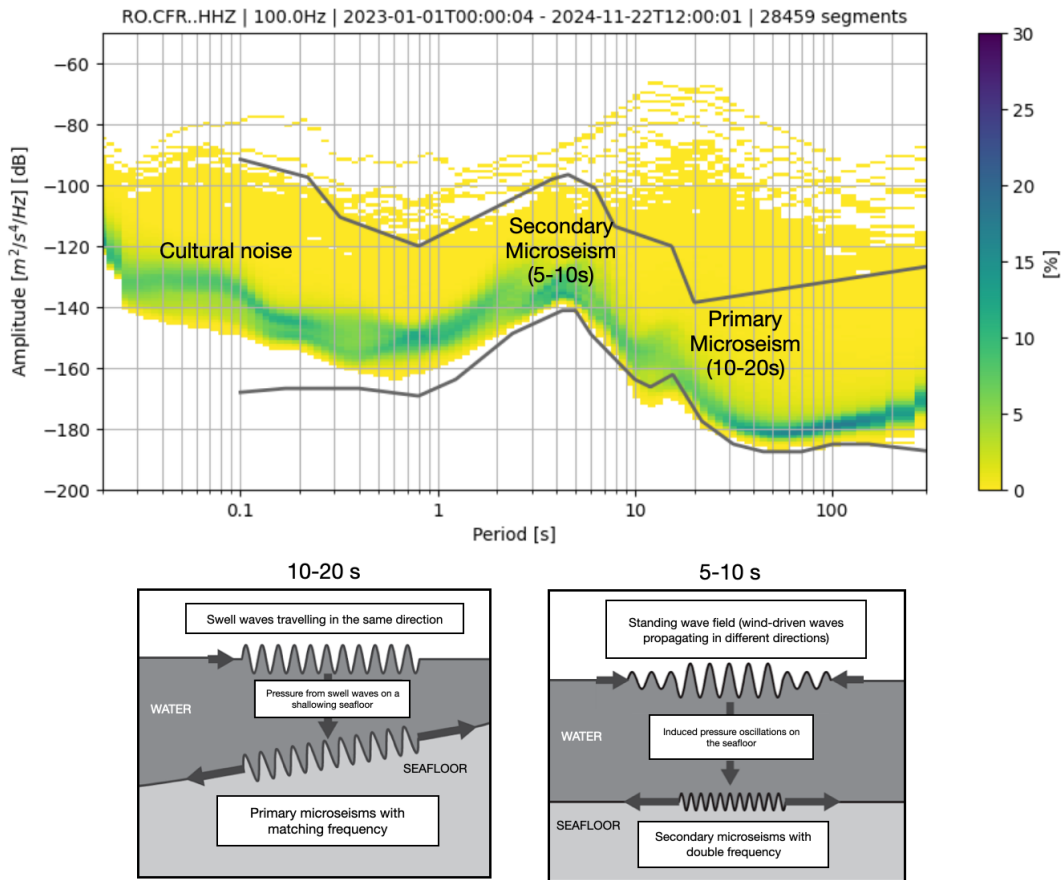
132
 133 *Figure 2. a. Map of Europe and the Black Sea coast showing GNSS stations and their belonging networks*
 134 *used for analysis in this study. b. Map of the Romanian sea coast showing seismic stations (red triangles)*
 135 *and the location of the AGIR infrasound array (star). Coloured contours represent total wave height at*
 136 *18:00 UTC on the 30th of August 2024 from ERA5 reanalysis data. c. The layout of the AGIR infrasound*
 137 *array.*

138
 139 **3.1 Seismic Data**

140 Seismic data represents vibrations of the Earth's surface, commonly referred to as seismic noise.
 141 These low-amplitude movements are recorded across the Earth's surface and are traditionally used
 142 to study the Earth's internal structure and detect earthquakes. Recently, it has increasingly found
 143 applications in meteorology and hydrology, particularly for monitoring weather events (e.g. Dias
 144 et al. 2023; Hua et al., 2023), destructive flood episodes (Burtin et al., 2016), ocean storms, and
 145 tropical cyclones (Gualtieri et al., 2018). Seismic noise can reveal the impact of atmospheric and
 146 oceanic conditions, providing valuable insights into weather events and climate changes (e.g.
 147 Bromirski et al., 2002; Aster et al, 2008; 2023). In particular, seismic data helps track variations
 148 in the Earth's surface caused by factors such as ocean waves, wind, and precipitation, offering a
 149 unique perspective on these phenomena (e.g. Grevemeyer et al., 2000; Borzi et al., 2022).

150 When the seismic noise is analyzed in the frequency domain, two clear peaks emerge in the
 151 spectrum (Figure 3), reflecting distinct types of ocean wave interactions (Koper et al., 2015;

152 Arduin et al., 2019; Tanimoto et al., 2023). The primary peak, observed in the range of 10-20
 153 seconds (0.05-1 Hz), is generated by the impact of "swell" waves traveling in the same direction,
 154 inducing pressure variations in the Earth's crust that match the period of the waves. The secondary
 155 peak, in the range of 5-10 seconds (0.1-0.5 Hz), is produced by wind-driven waves, which
 156 propagate in different directions and generate pressure oscillations on the ocean floor (Ebeling et
 157 al., 2012). These seismic signals directly link ocean conditions with seismic activity (Li et al.,
 158 2020), providing insights into large-scale weather phenomena like ocean storms.



159
 160 *Figure 3. Probabilistic Power Spectral Density (PPSD) of seismic noise for station CFR, over two years,*
 161 *showing key sources of primary and secondary microseisms. Below, sketches illustrate the generation*
 162 *mechanisms: primary microseisms are caused by unidirectional swell waves inducing pressure fluctuations*
 163 *on a shoaling seafloor, while secondary microseisms result from nonlinear interactions of wind-driven*
 164 *waves over deeper water (modified after Ebeling, 2012).*

165 Higher frequencies above 30 Hz are associated with the effects of precipitation and wind, as seen
 166 in studies like Rindrharisaona et al. (2022) or Diaz et al. (2023). These higher-frequency seismic
 167 signals help track more localized weather events, such as storms and heavy rainfall. Seismic data,
 168 when integrated with other meteorological tools, enhances the ability to monitor and predict
 169 weather events.

170 To analyse seismic data, the raw traces are first corrected for instrument response and converted
171 to units of velocity. These are then filtered with bandpass butterworth filters adapted to capture the
172 target signal: low pass filtering (<1 Hz) for wave-seafloor coupled interactions and high pass
173 filtering (>30 Hz) to identify possible signatures of precipitation, essentially induced pressure
174 fluctuations in the ground converted to weak seismic vibrations due to rain drops. Spectrograms
175 of these filtered seismic traces were computed using short-time Fourier transforms implemented
176 in the `scipy.signal` package, with the default 256-sample window length used for each segment,-to
177 visualise signatures of the hydro-meteorological phenomena in the frequency content of ground
178 vibrations.

179 Potential environmental signals in the seismic data were also investigated using power spectral
180 density (PSD) analysis. To account for variations over time, a Probabilistic Power Spectral Density
181 (PPSD) method was applied. The continuous waveform was divided into 1-hour time windows
182 with 50% overlap, and a PSD was computed for each window after instrument-response correction
183 and basic preprocessing. These estimates were combined into a probability distribution, providing
184 a statistical overview of typical and transient noise levels across frequencies. The PPSD was
185 produced using ObsPy (Beyreuther et al., 2010), which handles data gaps and ensures reliable
186 normalization.

187 Temporal variations in PSD amplitudes are also analyzed to track changes in seismic noise at
188 specific frequencies. By extracting PSD values at selected frequencies that are expected to capture
189 primary and secondary microseisms, time series of noise levels are generated. These temporal
190 PSDs allow for the identification of trends and correlations with environmental factors, such as
191 ocean wave activity or weather conditions.

192 **3.2 Acoustic Data**

193 Infrasound waves are low-frequency acoustic waves that are inaudible to the human ear, typically
194 below 20 Hz. These waves are generated by a variety of natural and anthropogenic sources,
195 including meteorological events, volcanic eruptions, earthquakes, and human activities such as
196 explosions and industrial processes (Campus and Christie, 2009; Bondár et al., 2022). In particular,
197 infrasound is often associated with phenomena like thunderstorms, ocean waves, and large-scale
198 atmospheric events, which generate pressure fluctuations that propagate through the atmosphere
199 (e.g. Stopa et al., 2012; Landès et al., 2012; Listowski et al., 2022). These waves provide valuable
200 information about the dynamics of weather systems (e.g. Hupe et al., 2019), making them an
201 essential tool for monitoring and understanding environmental processes (e.g. Brachet et al., 2009;
202 Hupe et al., 2022). Infrasound associated with thunderstorms, primarily generated by acoustic
203 waves from thunder, has been studied previously and shown to be detectable at distances ranging
204 from tens to hundreds of kilometers (e.g., Assink et al., 2008; Sindelarova et al., 2015; Šindelářová
205 et al., 2021). Nevertheless, infrasound arrays detect signals from multiple storm-related sources,
206 not just thunder (e.g., Waxler et al., 2024). In the present study, we build on this understanding by
207 integrating these signals with seismic, satellite, meteorological, and water vapor observations to
208 investigate what these complementary datasets reveal about storm evolution in a coastal
209 environment.

210 For the monitoring of infrasound signals, we use data from an infrasound array system located at
211 Eforie Nord-Agigea, Romania (AGIR, Figure 2). This array consists of multiple sensors, including

212 SIS-1 infrasonic sensors (Seismowave), equipped with global positioning systems (GPS) and noise
213 reduction technology.

214 To analyze the seismo-acoustic characteristics of the August 30-31 Black Sea storm, we used a
215 two-pronged approach: (1) single sensor signal analysis based on feature extraction and
216 unsupervised machine learning, and (2) array-based analysis using all the sensors of AGIR and
217 classic multi-channel correlation algorithms. Together, these methods provide complementary
218 insights into the acoustic behavior of the storm, capturing both local signal characteristics and
219 spatial coherence across sensors.

220 For the single-station analysis, infrasound data recorded at the AGIR sensor (Figure 2) was
221 segmented into 30-minute windows, and a set of time-frequency features was extracted to
222 characterize the signal dynamics (Supplementary Material). These features describe how energy
223 and frequency content evolve over time, providing insights into the structure of the infrasound
224 signal. Parameters such as spectral centroid and spectral rolloff are standard descriptors in acoustic
225 signal analysis and are suitable here because they effectively capture shifts in dominant frequency
226 produced by lightning-generated acoustic waves or the passage of pressure disturbances, while
227 spectral flux highlights changes in broadband acoustic energy (Pásztor et al., 2023). Spectral
228 entropy reflects the complexity of the frequency distribution, which increases during turbulent
229 atmospheric conditions, and the zero-crossing rate, mean, and variance of the power spectrum
230 summarize overall activity and variability. This feature set provides a compact representation of
231 the signal suitable for unsupervised machine-learning approaches such as clustering, techniques
232 widely used in data mining to identify patterns in multidimensional time-frequency data (e.g.,
233 Coates and Ng, 2012), and allows us to distinguish physically interpretable stages of storm-induced
234 changes in the infrasound wavefield.

235 The extracted features were used as input for K-Means clustering (MacQueen, 1967), an
236 unsupervised machine learning algorithm that partitions data into a predefined number of groups.
237 K-Means minimizes within-cluster variance by iteratively assigning feature vectors to the nearest
238 cluster centroid and updating the centroids based on the grouped data. This clustering method
239 enables the identification of distinct acoustic patterns in the signal (e.g. Pásztor et al., 2023),
240 offering a data-driven way to segment the storm’s infrasound profile without requiring prior labels
241 or assumptions. Prior to clustering, the features were standardized using z-score normalization, to
242 ensure comparable scaling across variables. The optimal number of clusters was determined using
243 the elbow method, which evaluates within-cluster variance as a function of cluster number
244 (Supplementary Material). To select the most informative features, we applied covariance pruning,
245 and the temporal evolution of the features was visualized to ensure meaningful representation. This
246 procedure resulted in six clusters, providing a balanced representation of the infrasound dynamics
247 while avoiding over-segmentation or overfitting. By combining multiple features in the clustering,
248 this method captures the evolving acoustic states of the storm in a compact, interpretable form.

249 In parallel with the single-station analysis, we also applied the Progressive Multi-Channel
250 Correlation (PMCC) method, as implemented in the DTK-PMCC software (Cansi and Le Pichon,
251 2008; Le Pichon et al., 2010) to detect and analyze coherent acoustic signals across an infrasound
252 array. The PMCC method targets signals generated by atmospheric sources such as lightning (i.e.,
253 associated thunders) or other pressure disturbances, operating in the low-frequency range of 0.7 to

254 7 Hz. It is specifically suited for mini-array configurations, where signal coherence between
255 closely spaced sensors can be exploited for precise signal detection and characterization.

256 The PMCC algorithm was implemented using a multi-resolution configuration following the
257 standardization proposed by Garcés (2013), with window lengths and frequency bands arranged
258 in third-octave bands. A total of 19 frequency bands were used, covering 0.1-7 Hz. Window
259 lengths decrease logarithmically with frequency, ranging from 258 s in the lowest band to 4 s in
260 the highest band. A 10% time step was applied (corresponding to 90% overlap between
261 consecutive windows), and this scheme repeats every decade. Within each time-frequency
262 segment, cross-correlations are computed between all sensor pairs to identify coherent wavefronts,
263 signals that exhibit consistent arrival times across the array. From these detections, PMCC
264 estimates several key propagation parameters, including backazimuth (the direction of arrival),
265 horizontal trace velocity, amplitude, duration, and dominant frequency. This approach is
266 particularly effective in noisy environments and enables the discrimination of storm-generated
267 infrasound from background signals or unrelated acoustic sources. The algorithm's output consists
268 of a time-frequency map of signal detections enriched with physical metadata, allowing for
269 detailed interpretation of the storm's acoustic footprint and its temporal evolution.

270 3.3 Satellite Observations

271 We also incorporated data from the Meteosat Third Generation (MTG) satellite system (Holmlund
272 et al., 2021), specifically from its Lightning Imager (LI) sensor (Viticchie et al., 2020). The MTG
273 satellites operate in geostationary orbit at approximately 36,000 km altitude, providing continuous
274 observations over Europe, Africa, and surrounding waters. The Lightning Imager detects cloud-
275 to-cloud, cloud-to-ground, and intra-cloud lightning flashes using four cameras that collectively
276 cover 86% of the Earth's visible disc from the satellite's perspective.

277 For this study, we used Level 2 group data, which includes the geographical coordinates and timing
278 of each detected flash. The MTG Lightning Imager detects total lightning (cloud-to-cloud and
279 cloud-to-ground) optically at 777 nm, with 4.5 km pixel resolution at the sub-satellite point and
280 1 ms frame rate (Holmlund et al., 2021; Kokou, 2023). Level-2 achieves detection efficiencies of
281 ~80-90%, capturing even weak flashes reliably, with false alarm rates <0.3 (Enno et al., 2025).
282 Flash geolocation uncertainty reaches 5-10 km near the edge of the instrument's field of view,
283 where off-nadir viewing geometry amplifies parallax effects (Bližňák & Sokol, 2026). By mapping
284 these detections, we were able to analyze the spatial distribution and temporal evolution of the
285 storm's lightning activity. The dataset also offered insights into the storm's intensity and structure,
286 complementing other meteorological observations.

287 Associations between infrasound detections and lightning flashes detected by MTG within 50 km
288 of the AGIR infrasound station were investigated by assuming direct-path acoustic propagation
289 and a correspondence between infrasound time-of-arrival and the MTG lightning discharge time
290 (after Assink et al., 2008):

$$291 t = t_{\text{MTG}} + d/c + \Delta t,$$

292 where d is the distance between the lightning discharge and the infrasound station, $c = 340\text{m/s}$,
293 and $\Delta t = \pm 10\text{s}$ accounts for timing uncertainty associated with the simplified propagation

294 assumption. In particular, infrasound travel time from thunder sources can vary due to atmospheric
295 temperature and wind variations along the propagation path, which affect the effective sound speed
296 and may introduce deviations from the assumed constant-velocity, straight-path propagation.
297 Additionally, a maximum angular deviation of 10° between the observed infrasound backazimuth
298 and the MTG-derived backazimuth is permitted for an association to be accepted.

299 **3.4 GNSS Data**

300 The use of GNSS technology for atmospheric monitoring provides a powerful tool for analyzing
301 extreme weather events. Beyond its well-known applications in navigation, timing, positioning
302 and crustal dynamics (Nistor et al., 2021a; Nistor et al., 2021b), GNSS has become a reliable
303 method for sensing tropospheric water vapour, an essential driver of weather systems and a key
304 variable in forecasting models (Guerova et al., 2016; Vaquero-Martínez and Antón, 2021). Over
305 the past two decades, ground-based GNSS networks in Europe have contributed significantly to
306 operational meteorology by providing near real-time estimates of atmospheric water vapour,
307 aiding in the detection and tracking of severe weather, including heavy rainfall and storms
308 (Karabatić et al., 2011; Priego et al., 2017; Jones et al., 2020). These high-resolution observations
309 have proven valuable for both nowcasting and validating numerical weather prediction models
310 (Wilgan et al., 2015; Bosy et al., 2012; Awange, 2012).

311 In this study, GNSS data were collected from several networks (Figure 2), including the
312 International GNSS Service (IGS, Johnston et al., 2017), the EUREF Permanent Network (EPN,
313 Bruyninx et al., 2012), the Romanian Position Determination System (ROMPOS, Iliescu et al.,
314 2019), and GEOPONTICA (Dimitriu et al., 2017). A total of 37 permanent GNSS stations were
315 analyzed over a 30-day period, with the rainiest interval selected at the midpoint of the study
316 period. These stations provide high-quality, continuous observations critical for atmospheric
317 monitoring.

318 The data were processed using a double-differenced, ionosphere-free combination of L1 and L2
319 carrier phases. This approach helps minimize errors such as ionospheric delays, satellite clock
320 biases, and other common atmospheric effects. The resulting Zenith Tropospheric Delay (ZTD)
321 values were then corrected using the Vienna Mapping Functions 3 (VMF3, Landskron et al., 2018),
322 which improves the accuracy of ZTD by accounting for variations in the troposphere's atmospheric
323 conditions. Once the ZTD was refined, it was converted into integrated precipitable water vapor
324 (PWV) using surface meteorological data (temperature and pressure) from co-located weather
325 stations, following the method outlined by Bosy et al. (2012). This process allowed for the
326 derivation of high-resolution atmospheric water vapor content, critical for analyzing the dynamics
327 of the extreme storm event over the Black Sea. By combining GNSS-derived PWV with data from
328 other observational sources, the study captured the temporal and spatial variations in atmospheric
329 moisture, offering valuable insights into the storm's development and intensity.

330 **3.5 Meteorological Data**

331 To compare the infrasound signals captured during the Black Sea extreme storm event, we
332 extracted meteorological data from the open-access ERA5 reanalysis dataset, produced by the
333 European Centre for Medium-Range Weather Forecasts (ECMWF). This dataset provides a
334 comprehensive record of global weather conditions from 1950 to the present (Hersbach et al.,

335 2023). ERA5 combines observational data and advanced numerical models to generate relatively
336 high-resolution atmospheric parameters compared with earlier global reanalyses, including
337 precipitation (Figure 1), wind speed, and wave height. ERA5 has been extensively validated (Jiao
338 et al., 2021; Wu et al., 2022; Soci et al., 2024) and is widely used in studies of storm evolution and
339 precipitation dynamics (e.g. Dullart et al., 2020; Tiberia et al., 2021; Price et al., 2025), making it
340 a suitable choice for the mesoscale processes examined here.

341 For our study, the ERA5 data was used to track the meteorological context of the storm, offering
342 insights into the intensity of precipitation, the evolution of wind patterns, and the development of
343 oceanic wave heights. With a temporal resolution of 1 hour and spatial resolution of $0.25^\circ \times 0.25^\circ$,
344 ERA5 allows for a mesoscale comparison of the storm's meteorological characteristics over time.
345 While its spatial averaging cannot resolve localized convective-scale precipitation, it provides a
346 vital benchmark for qualitative comparisons and for testing multi-sensor monitoring potential.
347 These comparisons help us understand the storm's dynamics and assess its impact, further
348 enhancing the interpretation of infrasound signals and aiding in future storm prediction and
349 monitoring efforts. The open-access nature of ERA5 ensures broad accessibility, contributing to
350 the transparency and reproducibility of our storm analysis (Copernicus Climate Change Service,
351 Climate Data Store, 2023).

352 **4. Results**

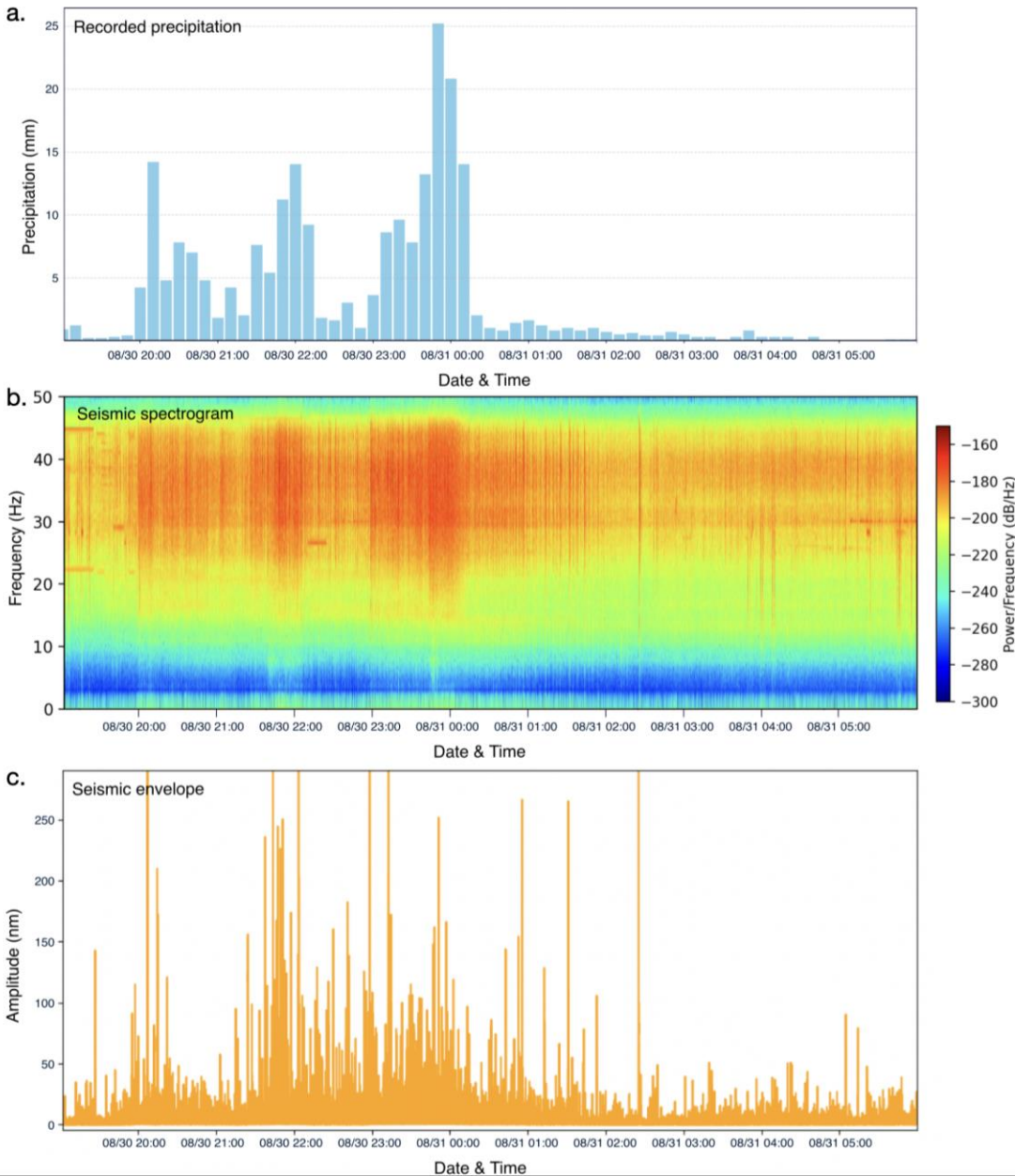
353 **4.1 Seismic signatures of storm evolution**

354 High frequency (>30 Hz) analysis of seismic noise reveals strong signals during periods of intense
355 rainfall (Figure 4). Specifically, the displacement envelope at station MANR and its spectrogram
356 for 30 August, 12:00 UTC to 31 August, 06:00 UTC (Figures 4b, c) reveal strong signal around
357 midnight, when recorded precipitation exceeded 20 mm per 10 minutes. Similar temporal patterns
358 in the seismic spectrogram were also visible when compared with hourly precipitation levels from
359 ERA5, indicating that the high amplitude of energy observed above 30 Hz is most plausibly
360 generated by raindrop impacts.

361 However, this correspondence is not uniform across all rainfall episodes. While the main
362 precipitation maximum on 30-31 August produces a clear and sustained seismic response, several
363 lower-intensity precipitation pulses show a much weaker or no recognizable signature in either the
364 seismic envelope or spectrogram. This behaviour is consistent with previous work (e.g.,
365 Rindraharisaona et al., 2022), which demonstrates that only rainfall above a certain intensity, or
366 involving sufficiently large drops, generates impact forces strong enough to be detected by
367 broadband seismometers. Our observations therefore reflect both strong positive correlations
368 during intense rainfall and the lack of seismic expression for weaker precipitation. This selective
369 sensitivity supports the interpretation that high-frequency seismic noise can reflect strong rainfall
370 peaks but is less responsive to light or moderate precipitation, an important nuance when
371 interpreting multi-sensor relationships in this study.

372 Anthropogenic seismic noise is typically strongest at low to mid frequencies (<25 Hz), where day-
373 night variations reflect traffic, human activity, and transient signals from machinery, while higher-
374 frequency bands (25-45 Hz) may include periodic contributions from rotating equipment (e.g.,
375 Gross & Ritter, 2008; Diaz et al., 2017). The bandwidth targeting rainfall in this case is between

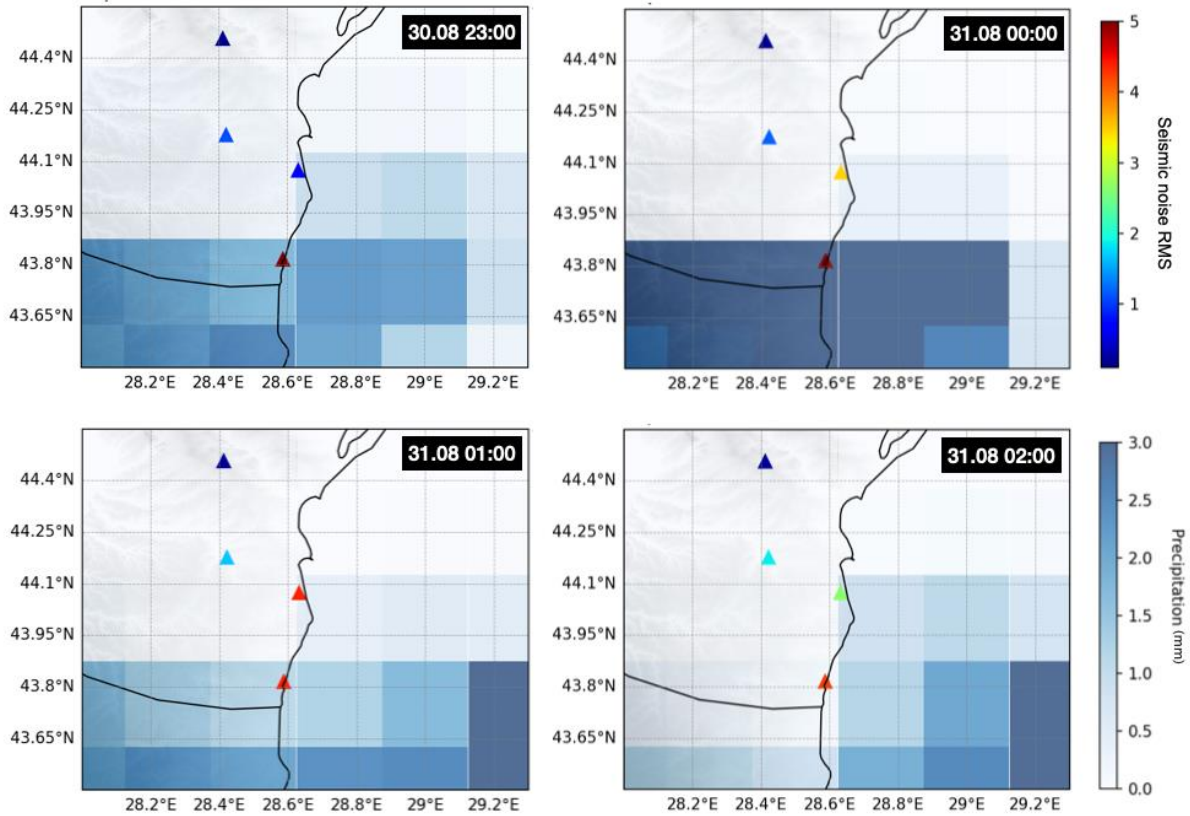
376 30-50 Hz, which is above the dominant frequency content of most anthropogenic sources and
377 overlaps with raindrop-impact energy documented in recent rainfall-seismic studies.



378
379 *Figure 4. High frequency (30-50Hz) observations of the storm at station MANR. a. Time series of total*
380 *precipitation every 10 minutes from the ANM station at Mangalia b. Spectrogram of the seismic time series*
381 *for station MANR. c. Envelope of the displacement seismogram at station MANR.*

382 To visualise the signature of the storm passing over the network of broadband seismic stations in
383 the coastal area, we also plotted the hourly precipitation values with the hourly root-mean-square
384 amplitudes of the high-frequency (>30 Hz) seismic velocity envelopes recorded at seismic stations.
385 Figure 5 shows four snapshots of hourly plots of gridded precipitation data from ERA5, which
386 have a lower amplitude than point measurements at the Mangalia station, due to the averaging over

387 the grid block. This figure presents a temporal coincidence between changing precipitation patterns
 388 from ERA5 data and the amplitudes of high-frequency seismic noise. This observation further
 389 supports the likelihood of a causal relationship. These high-frequency seismic signals could
 390 potentially be explored as a near real time indicator of intense rainfall events, providing a
 391 conceptual basis for a simple streaming detection approach.



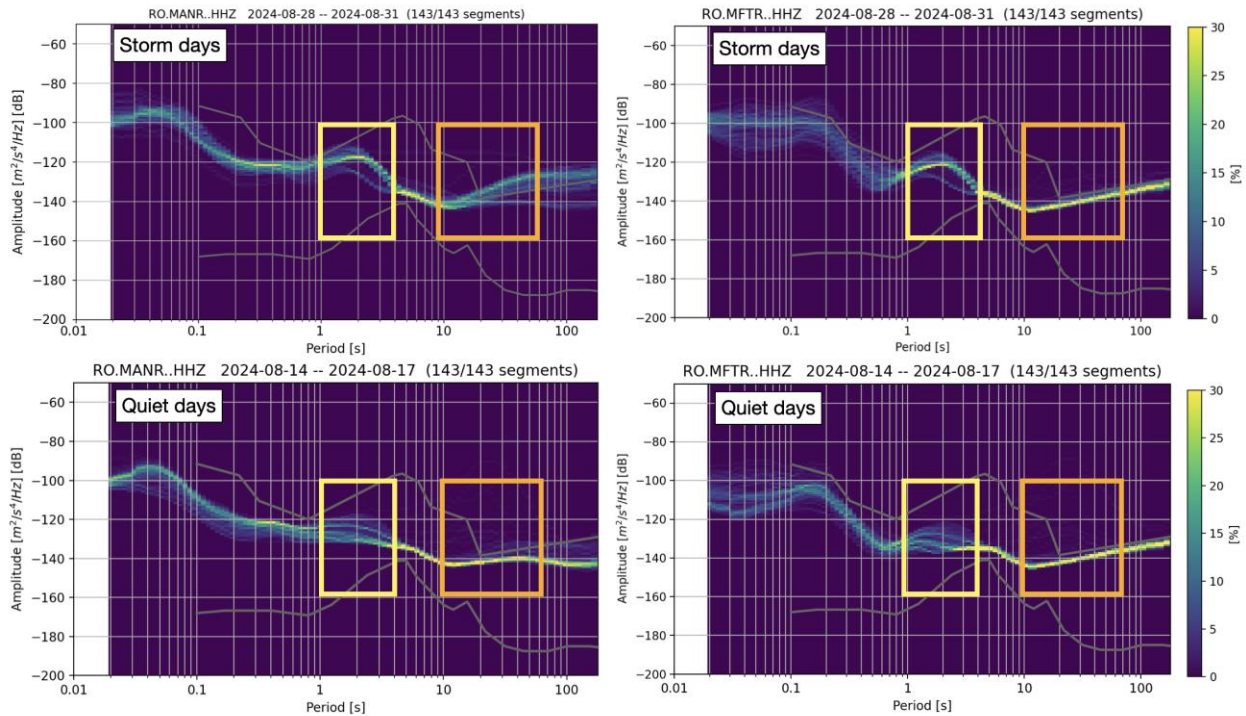
392
 393 *Figure 5. Distribution of hourly RMS of high pass filtered (>30 Hz) seismograms and precipitation data.*
 394 *Colours indicate hourly RMS amplitude of velocity envelopes filtered 30-50 Hz. Background coloured*
 395 *grid indicates the total precipitation (mm) from ERA5 data.*

396 The analysis of the microseismic noise frequency band is closely linked to the interaction between
 397 ocean waves and the seafloor, which is influenced by storm conditions. To assess the storm's
 398 impact, we analyze the PPSD (Probabilistic Power Spectral Density) of noise recorded at several
 399 stations during both storm and quiet days, using the latter as a baseline. Figure 6 shows examples
 400 of PPSD at stations MANR and MFTR (Figure 2), revealing differences in PSD amplitudes across
 401 the primary and secondary microseismic bands. These differences indicate the presence of high-
 402 intensity wind-driven waves and swell energy in the sea.

403 The secondary microseismic band, in particular, shows a significant rise in amplitude during
 404 storms, consistent with established mechanisms linking storm-driven wave activity and seafloor
 405 pressure fluctuations (Figure 3) to enhanced secondary microseism generation, while local factors
 406 such as bathymetry or wave direction may modulate the response (Bromirski et al., 2002; Ebeling

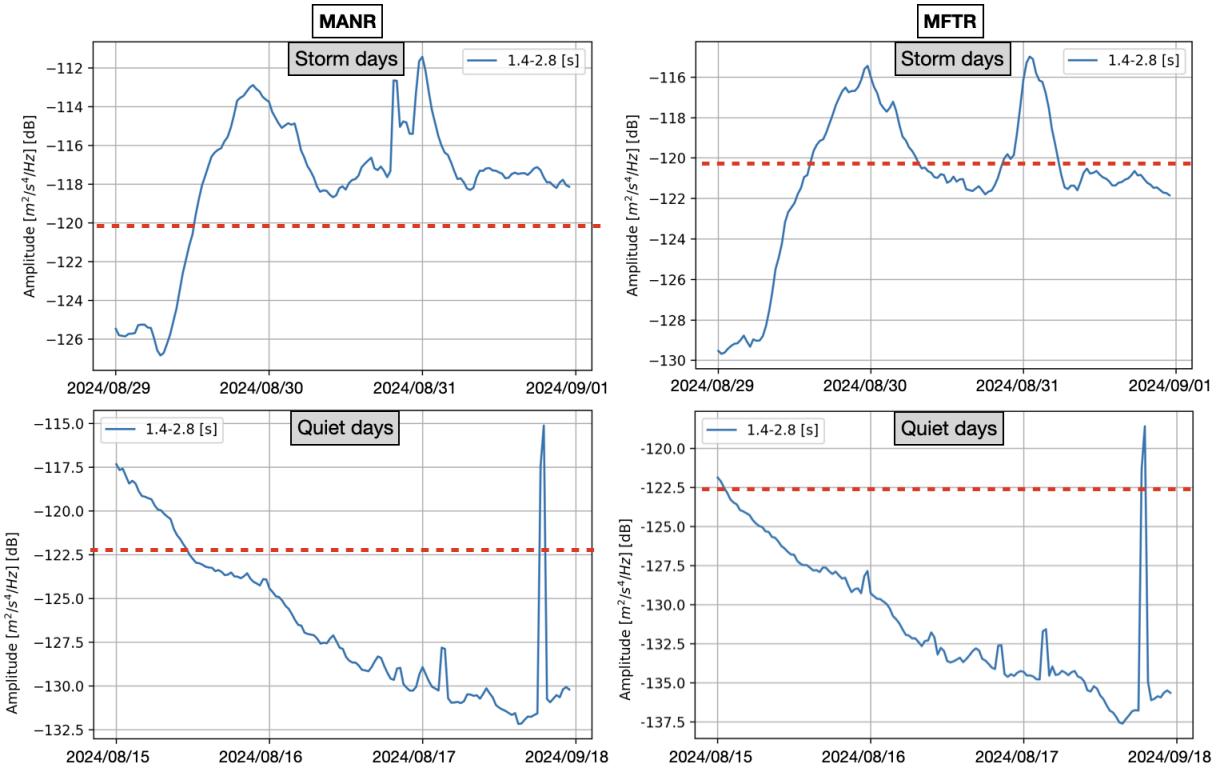
407 et al., 2012; Arduin et al., 2019). On quiet days, the PSD remains consistently lower, typically
 408 staying below the -120 dB threshold. This stark contrast emphasizes the role of atmospheric
 409 conditions in modulating seismic noise, with storms causing a notable increase in energy across
 410 both frequency bands. The temporal evolution of the PSD values (Figure 7) further highlights the
 411 storm's impact, with fluctuations corresponding to changes in environmental factors, reinforcing
 412 the connection between storm activity and the observed seismic signals.

413



414
 415 *Figure 6. Probabilistic Power Spectral Density (PPSD) plots for two seismic stations near the Black Sea*
 416 *coast capturing the target storm signal in the microseismic bandwidths (marked with rectangles). The top*
 417 *panels show the PPSD distributions across frequencies, indicating the probability of power spectral*
 418 *density values in percentage for days including the Black Sea storm. The bottom panels show PPSD for*
 419 *days with no recorded events.*

420 Anthropogenic seismic noise does not significantly affect the microseismic band (0.1-1 Hz).
 421 Human-generated vibrations predominantly occupy frequencies above 1 Hz, while long-period
 422 microseisms are produced by ocean wave interactions and are coherent over large distances. The
 423 temporal evolution of the microseismic energy observed in this study matches changes in wave
 424 state associated with the storm rather than any local activity. Similar to the findings of Gross &
 425 Ritter (2009), the sub-Hz frequency range is dominated by natural sources, with anthropogenic
 426 contributions being negligible.



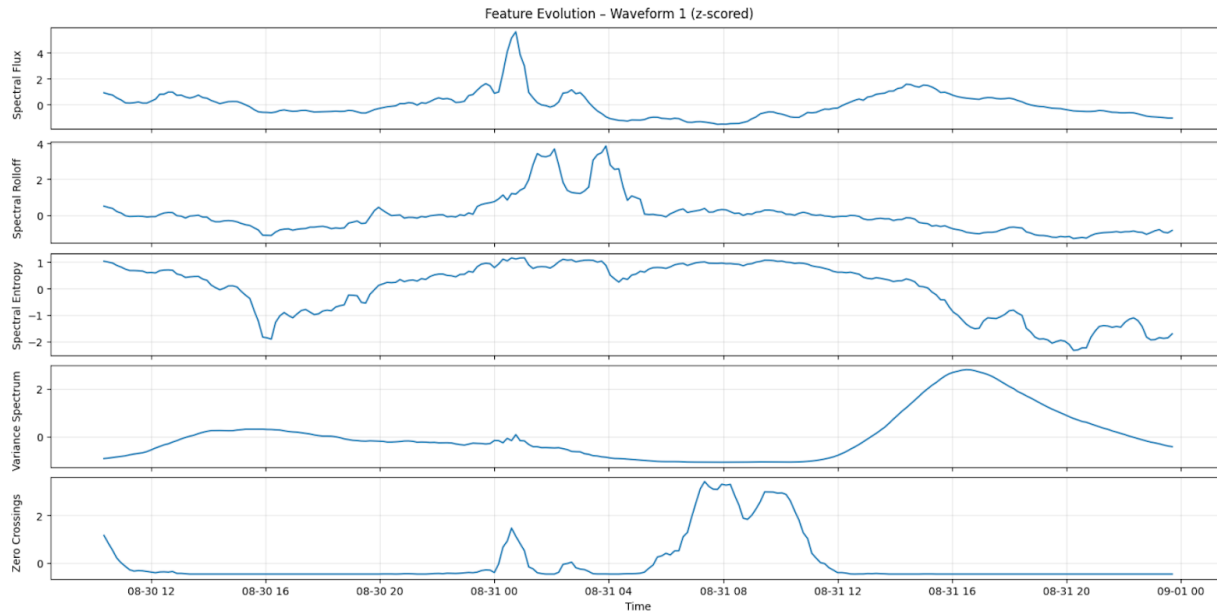
427

428 *Figure 7. Temporal PSDs for two seismic stations near the Black Sea Coast in the secondary microseismic*
 429 *band showing significantly higher values (>-120 dB) during stormy days compared to days without*
 430 *recorded precipitation.*

431 4.2 Infrasonic and satellite lightning observations

432 4.2.1 Single-station feature extraction

433 The evolution of time-frequency features over the duration of the Black Sea storm revealed distinct
 434 patterns in the infrasonic signal (Figures 8 and 9). Centroid and rolloff show parallel behavior
 435 because they are both frequency-domain descriptors tied to the distribution of spectral energy, and
 436 so both respond strongly to the same uplift in energy during the storm's peak. Spectral flux, by
 437 contrast, quantifies inter-frame spectral change, so its peak occurs where the spectrum transitions
 438 most rapidly, even when that does not coincide with the maximum absolute energy (e.g. Pásztor
 439 et al., 2023). Finally, the zero-crossing rate reflects time-domain volatility, not spectral shape,
 440 which explains its distinct pattern, such as the storm's later stages may introduce broadband
 441 turbulence or noise components that boost zero crossings independently of the spectral shifts
 442 visible in the first two panels. While the individual features varied over time, it is the combination
 443 of these features through K-means clustering that effectively identifies the time frame
 444 corresponding to the main precipitation episode. Zero-crossings exhibited more variable patterns,
 445 reflecting high-frequency fluctuations, but the joint clustering of all features robustly captures the
 446 timing of the storm's most intense phases.

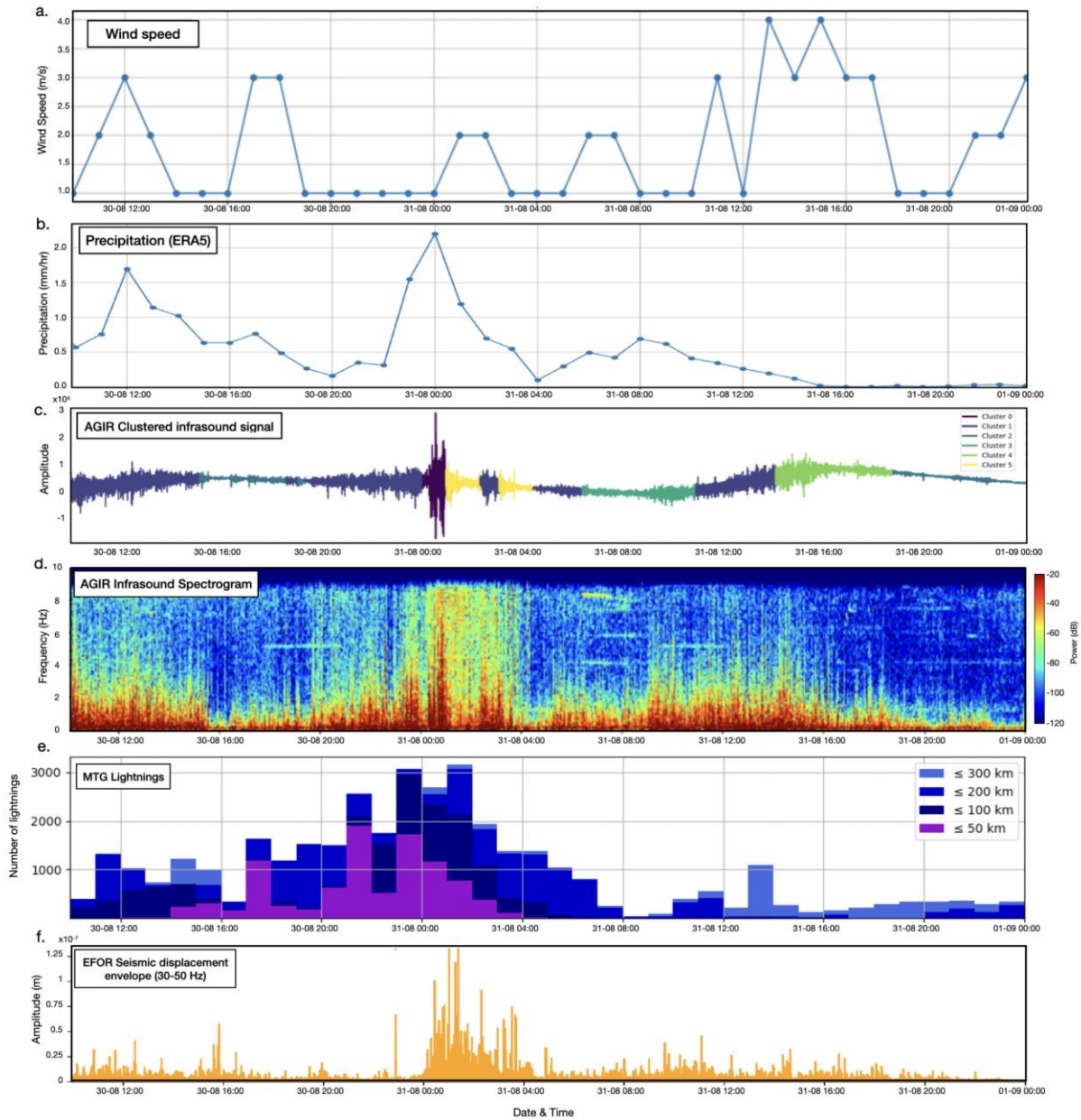


447

448 *Figure 8. Time-frequency feature analysis for the single-station infrasound signal recorded at AGIR during*
 449 *the Black Sea Storm.*

450 K-means clustering separated the acoustic data into six groups with distinct spectral and amplitude
 451 characteristics (Figure 9). These clusters highlight acoustic states that may relate to different
 452 environmental conditions during the monitoring period. For example, Cluster 0 coincides with
 453 periods of intense precipitation and stronger winds, and also aligns with enhanced lightning
 454 activity, suggesting a link with the most energetic phases of the convective system. Cluster 1
 455 captures intervals with moderate amplitudes but persistently elevated background acoustic levels,
 456 without corresponding rainfall or wind peaks, and with comparatively reduced lightning
 457 occurrence. Cluster 2 reflects calmer conditions with low amplitudes and little or no precipitation
 458 and minimal lightning activity. Transitional patterns also arise, such as Cluster 3, which appear
 459 before intervals grouped in Cluster 1 and mark intermediate acoustic activity. Overall, the
 460 clustering approach demonstrates that combining multiple features reveals consistent acoustic
 461 regimes and can help differentiate environmental conditions, without relying on any single
 462 parameter.

463 Interestingly, the spectral content of the infrasound signal showed similarities to seismic signal
 464 envelopes, particularly in the high frequency ranges (Figure 9), which may suggest a connection
 465 between the atmospheric pressure waves detected by infrasound and the ground vibrations
 466 captured by seismic instruments. When considered alongside the temporal evolution of lightning
 467 activity, this overlap implies that both seismic and infrasound signals could be complementary in
 468 capturing different aspects of storm dynamics, with seismic signals reflecting ground vibrations
 469 and infrasound capturing the atmospheric processes, and lightning indicating convective intensity.



470
 471 *Figure 9. Clustering results of infrasound signals recorded at AGIR from the August Black Sea storm event*
 472 *compared with precipitation data and seismic signal from EFOR station. a. Wind speed per hour measured*
 473 *at ANM meteorological station Constanta; b. Average precipitation data from $1^{\circ} \times 1^{\circ}$ around AGIR. c. Raw*
 474 *infrasound signal recorded at the AGIR sensor during the period of August 30–31, 2024, with different*
 475 *segments color-coded according to the cluster they belong to, based on K-means clustering of 30-minute*
 476 *time-frequency feature windows. d. The corresponding spectrogram generated using Blackman windowing*
 477 *with 128 samples and 70% overlap; e. Number of lightnings detected by the MTG satellite. f. Seismic*
 478 *displacement envelope at station EFOR, filtered between 30–50 Hz.*

479

480

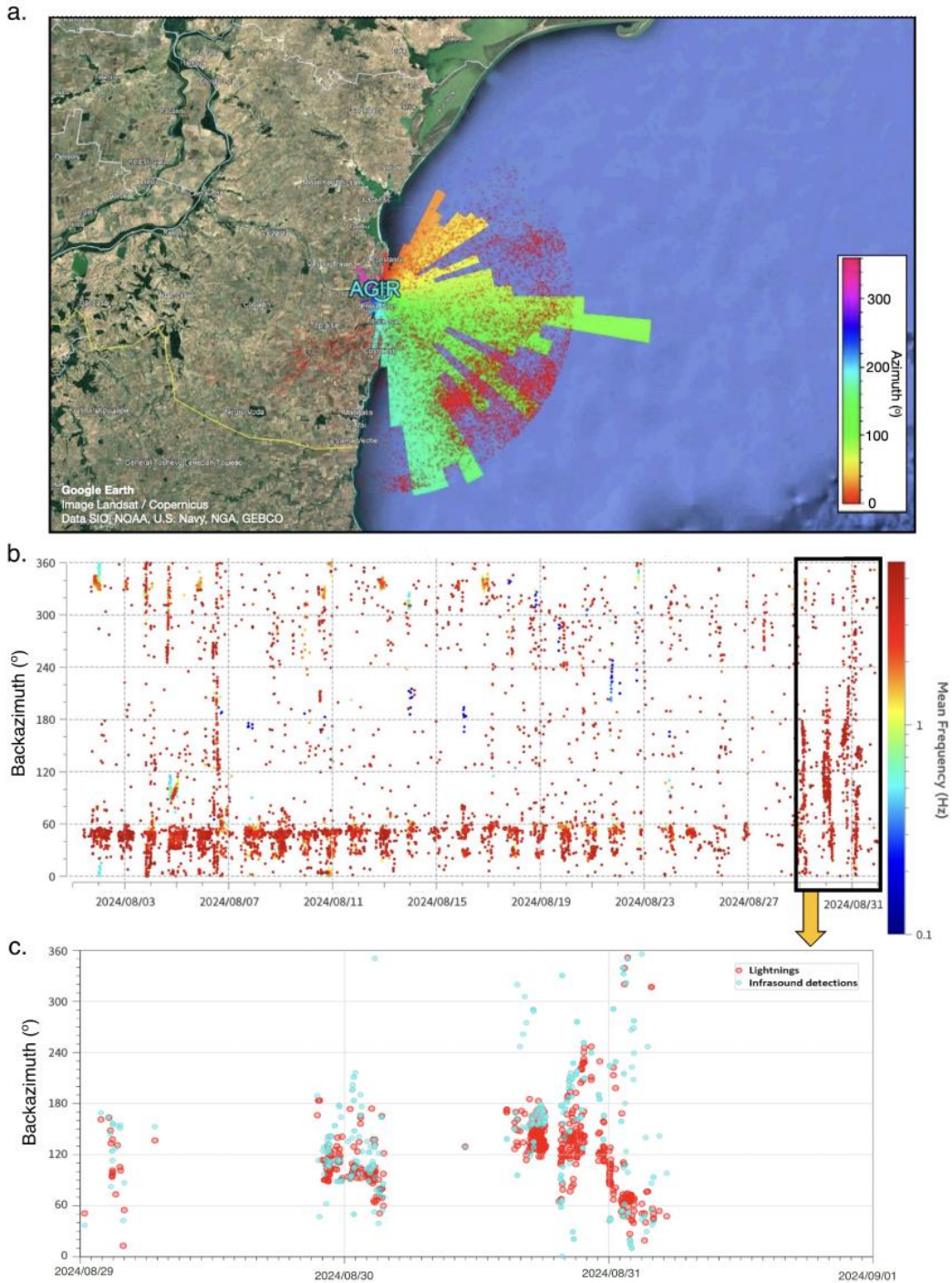
481

482 4.2.2 Array analysis and lightning detection

483 Using multiple sensors from the AGIR infrasound array with the PMCC algorithm allowed us to
484 isolate coherent infrasound signals and estimate their propagation parameters, such as backazimuth
485 and arrival times, across the sensor network. Nearly 11,000 lightning flashes were detected by the
486 MTG Lightning Imager within 50 km of the AGIR station during the Black Sea storm (Figure
487 10a), providing a dense reference set for comparison. Within the relevant 0.6-7 Hz frequency band,
488 approximately 1,100 infrasound detections were identified. These signals primarily consisted of
489 long-duration wave trains with frequent amplitude peaks and short-lived disturbances
490 characteristic of lightning-generated infrasound. Their dominant frequency was around 3 Hz, and
491 amplitudes ranged from 0.01 to 3.4 Pa (Figure 10b).

492 A subset of the infrasound detections could be confidently associated with individual lightning
493 discharges based on temporal alignment and backazimuth consistency. Overall, we were able to
494 associate 6.4% of lightning flashes with infrasound detections at AGIR (Figure 10c). This level of
495 correspondence is reasonable given that only a subset of lightning discharges radiate infrasound
496 efficiently and that propagation strongly depends on altitude, source geometry, and atmospheric
497 conditions. Nevertheless, these coincident detections demonstrate that lightning-generated
498 infrasound was clearly recorded during the storm and that the PMCC-derived acoustic signatures
499 provide valuable insight into the evolution of electrical activity and storm dynamics.

500 Anthropogenic noise sources, such as wind turbines (e.g., Jakobsen, 2005), industrial machinery
501 (Gastmeier and Howe, 2008), and road traffic (Grafkina et al., 2019), are well-documented
502 challenges for infrasound studies because they often generate persistent, periodic, or tonal signals
503 that can mask natural atmospheric phenomena. The AGIR infrasound array used here is located in
504 a semi-rural setting, distant from major roads and industrial facilities, which reduces the likelihood
505 of local anthropogenic contamination. Several independent lines of evidence indicate that such
506 contamination is negligible in this case study. First, the strongest infrasound signatures occurred
507 during night-time hours, when human activity is minimal. Second, both the clustering and PMCC
508 analyses identify transient signals with energy peaking around ~ 3 Hz, which contrasts sharply with
509 the more continuous or harmonic spectral patterns typically produced by anthropogenic sources.
510 Third, the temporal alignment of these acoustic signatures with independent observations of
511 lightning and precipitation provides ~~strong~~ confirmation that the detected infrasound variability is
512 storm-related rather than anthropogenic in origin.



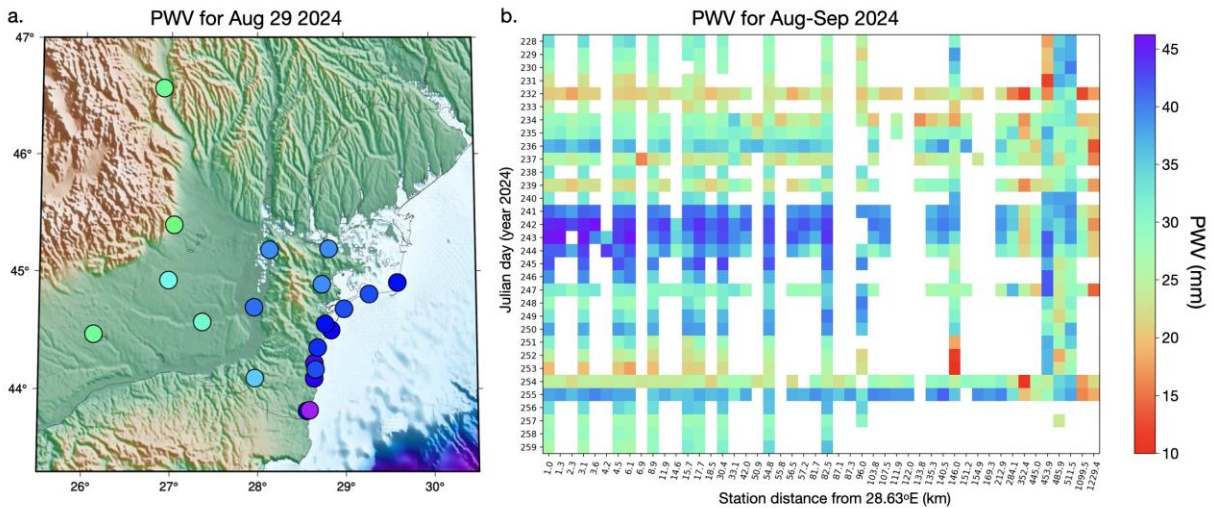
513

514 *Figure 10. a. Polar histogram of infrasound detections from the AGIR station, displayed with © Google*
 515 *Earth, along with the locations of lightning strikes detected by the MTG Lightning Imager system for the*
 516 *period from 29-31st of August 2024. The geographical position of the AGIR infrasound station is also*
 517 *shown on the map. b. diagram of high-frequency detections from the AGIR infrasound station between 1-*
 518 *31st of August 2024. c. Associations between events detected by the AGIR infrasound array and the MTG*
 519 *satellite database for 29-31st of August 2024.*

520 **4.3 GNSS-derived precipitable water vapor trends**

521 The analysis of daily GNSS-derived precipitable water vapor (Figure 11) reveals clear temporal
522 variations, with the highest PWV values consistently recorded on stormy days (>40 mm on DOY
523 240-243, i.e. August 27-30). Notably, the peak values occurred between DOY 241 and DOY 243
524 (Figure 11b), when the heaviest rainfall was observed (Figure 1). Coastal stations showed
525 extremely high PWV values (>40 mm) compared to inland stations (<30 mm), with a slight
526 decrease in PWV away from the coast (Figure 11a). This spatial distribution highlights the
527 geographical gradient of atmospheric moisture, with the highest PWV concentrations near coastal
528 areas, also decreasing gradually toward the north away from the storm peak. Interestingly, some
529 inland stations (BUCU, PGNL, RMSR) recorded their peak PWV on DOY 255, corresponding to
530 the onset of the Boris storm, another significant extreme rainfall event that swept through Central
531 and Eastern Europe (Athanasé et al., 2024).

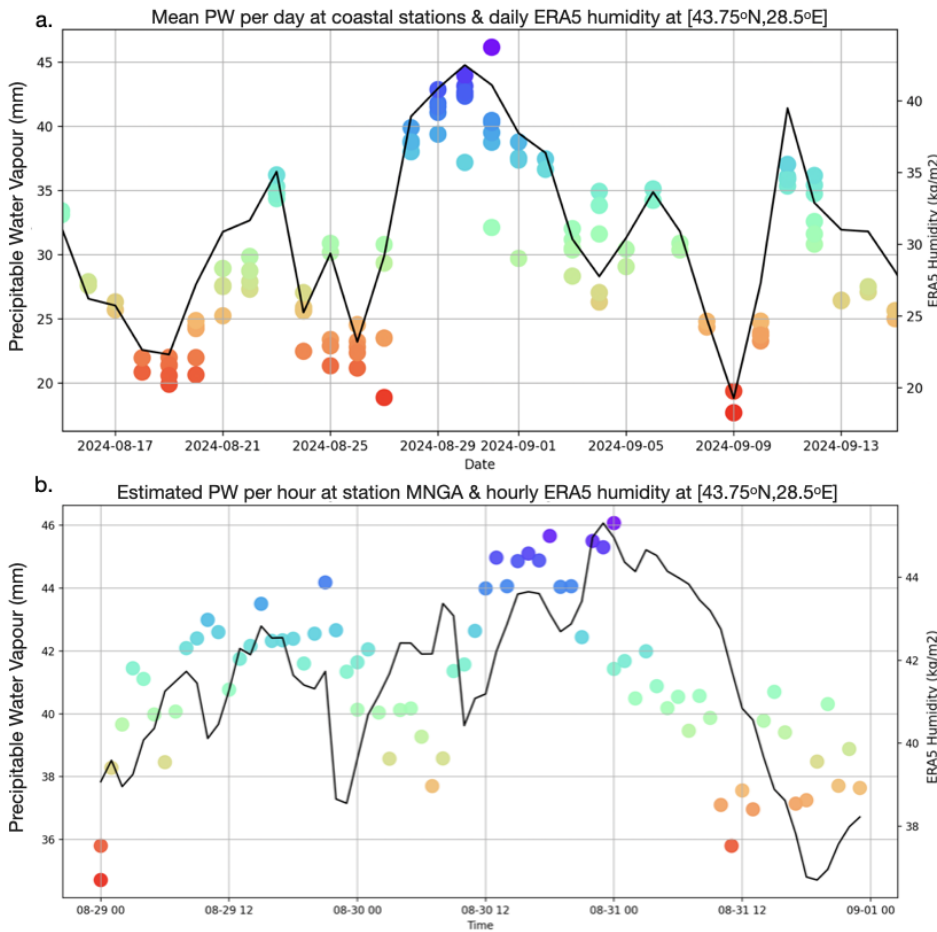
532 Elevated PWV was observed as early as August 27th (Figure 12a), suggesting that the tropospheric
533 moisture loading began to increase several days before the onset of the rainfall. This increase in
534 PWV may act as an indicator of a developing weather system. Remarkably, although HAR1,
535 located inland, did not directly experience the extreme rainfall, it exhibited similar PWV behavior
536 to coastal stations, suggesting that GNSS stations, even outside the immediate storm zones, can
537 capture atmospheric signals indicative of intense precipitation. This finding offers a valuable
538 precedent, showing that PWV measurements at GNSS stations not directly in the storm path can
539 still provide critical insights into moisture dynamics at the tropospheric level. The comparison
540 with ERA5’s total-column water vapour further supports this interpretation, as the broad temporal
541 evolution of ERA5 humidity mirrors the GNSS-derived daily PWV patterns, despite the inherently
542 coarser resolution of the reanalysis data.



543
544 *Figure 11. a: Map of GNSS stations coloured as a function of PWV estimated for the 29th of August. b.*
545 *Daily PWV values for each station, plotted as a function of their longitudinal distance relative to 28.63°E.*

546 Using the hourly PWV data, Figure 12b illustrates the evolution of water vapour at the MNGA
547 station, which recorded the heaviest rainfall in the study area. Notably, MNGA also showed a rapid

548 buildup of PWV, reaching values greater than 44 mm just a few hours before the storm event. This
 549 rapid increase in PWV suggests that the accumulation of atmospheric moisture may precede to
 550 extreme weather events, such as intense rainfall and storms. This observation aligns with known
 551 atmospheric dynamics, where a significant increase in water vapor content precedes heavy
 552 precipitation, highlighting the potential usefulness of GNSS-based PWV monitoring for studying
 553 pre-storm atmospheric moisture variability. The general rising trend toward the event is present in
 554 both GNSS-based and ERA5 reanalysis datasets, although some minor fluctuations are not
 555 matched. After the storm, the GNSS PWV drops sharply while ERA5 maintains elevated values
 556 for several hours. These differences show that GNSS can resolve rapid, real-time atmospheric
 557 changes that may be blurred in large-scale weather model products.



558

559 *Figure 12. Comparison of GNSS-derived precipitable water vapor (coloured circles) with independent*
 560 *humidity data (black line) from ERA5's total column vertically integrated water vapor parameter. a. Mean*
 561 *PWV values per day at selected GNSS stations (CONB, HARI, MNGA, MNGL, MNGM, TUZL) alongside*
 562 *daily averaged ERA5 humidity. b. Estimated PWV values per hour at the MNGA GNSS station compared*
 563 *with hourly ERA5 humidity at the 43.75°N, 28.5°E grid point. In both panels, GNSS data points are*
 564 *represented by colored circles where the color scale corresponds to the PWV magnitude, consistent with*
 565 *the vertical axis.*

566 **5. Discussion**

567 Storm evolution, in the meteorological sense, describes the sequence of processes from pre-storm
568 atmospheric moisture accumulation to convective initiation, peak rainfall, electrical activity, and
569 the associated marine response along coastal areas. The multi-sensor dataset used here captures
570 these different stages: GNSS-PWV documents the build-up of column water vapor before
571 convective onset, infrasound detects lightning-generated acoustic waves and pressure disturbances
572 during the mature convective phase, high-frequency seismic noise reflects the timing and spatial
573 progression of intense rainfall at the surface, microseisms respond to storm-driven changes in sea
574 state, and ERA5/MTG provide the mesoscale structure that ties these geophysical signals together.
575 By observing the same storm through these complementary physical pathways, we can outline a
576 more detailed picture of how the storm developed, intensified, and decayed than is possible from
577 individual datasets.

578 The integration of infrasound, seismic, and GNSS data in monitoring the extreme storm event over
579 the Black Sea provides valuable insights into the dynamics of storm behavior and illustrates the
580 potential of repurposing non-conventional sensors for meteorological analysis. Infrasound data,
581 for instance, revealed a clear acoustic signature of lightning activity, with signals detected in the
582 range of 0.6 to 7 Hz corresponding to electrical discharges. The high frequency of infrasound
583 detections (around 1,100) suggests that it may provide useful information for tracking storm-
584 related phenomena, particularly lightning, which is difficult to capture with traditional methods.
585 However, the signals did not always perfectly align with lightning strikes, indicating that other
586 factors, such as the movement of storm systems or variations in atmospheric conditions, may
587 influence infrasound signatures. This suggests that refining the correlation between infrasound
588 signals and lightning activity could be an avenue for future research, particularly in cases of sparse
589 lightning or in remote regions.

590 Seismic data alone also showed a strong connection between high-frequency seismic noise and
591 heavy rainfall, supporting previous studies that linked seismic signals to rainfall intensity. The
592 distinction between high-frequency and low-frequency seismic noise is particularly noteworthy.
593 Increases in high-frequency seismic noise occurred during intense precipitation, while low-
594 frequency signals were associated with wave height and storm-driven winds. This suggests that
595 different seismic frequencies capture distinct storm dynamics, with high-frequency signals
596 reflecting localized rainfall impacts and low-frequency signals tied to broader atmospheric and
597 oceanic interactions. This dual-frequency approach provides a more nuanced interpretation of
598 seismic data in storm monitoring, highlighting its complexity.

599 A key finding of this study is that K-means clustering of multiple acoustic features, including
600 spectral centroids, roll-off, flux, and zero-crossing rate, effectively segmented the infrasound
601 record into distinct storm phases. This approach proved more robust than relying on any single
602 feature, as the combination captured the complex, evolving nature of the storm's acoustic signature.
603 For instance, the identified clusters delineated periods of intense precipitation, elevated
604 background acoustic levels, and calm intervals, providing a data-driven overview of the storm's
605 progression. The fact that these acoustically defined phases align with independent meteorological
606 observations, such as rainfall peaks, confirms that the infrasound signal variability is a direct
607 response to the storm's atmospheric dynamics.

608 Furthermore, the observed spectral similarity between the infrasound signals and high-frequency
609 seismic envelopes suggests a coupled seismo-acoustic response to the storm. This implies that the

610 same atmospheric forcing, such as pressure fluctuations from rainfall and wind, generates
611 complementary signals in the atmosphere (infrasound) and the ground (seismic waves). Our
612 findings are consistent with other studies of intense weather systems, where coupled microbarom-
613 microseism signals have been shown to track storm structure and evolution (e.g., Butler & Aucan,
614 2018; Smirnov, 2021). The coherent acoustic and seismic responses to atmospheric-oceanic
615 pressures, as also documented in Distributed Acoustic Sensing studies (Taweessintananon et al.,
616 2023) and surf studies (Francoeur et al., 2025), reinforce the interpretation of a shared source
617 mechanism. Therefore, a major and logical next step is to move beyond analyzing these datasets
618 in parallel and to perform joint clustering of seismo-acoustic data (e.g. Floroiu et al., 2025). Such
619 an integrated approach could unlock a more comprehensive, multi-physics understanding of storm
620 dynamics by simultaneously characterizing the coupled atmospheric and ground-borne wavefields.

621 The temporal variations observed in GNSS-derived integrated precipitable water vapor provide
622 valuable insights into atmospheric moisture dynamics before extreme weather events. The
623 pronounced increase in PWV, particularly in the days leading up to and during the storm, supports
624 the link between elevated atmospheric water vapor and precipitation. Notably, the PWV buildup
625 starting roughly three days before the extreme rainfall suggests that rising moisture levels in the
626 troposphere were observed prior to the intense precipitation in this event. Even stations located up
627 to 130 km inland, such as HAR1, recorded similar PWV trends, indicating that GNSS stations
628 outside direct storm zones can still provide crucial atmospheric data. Hourly PWV trends further
629 revealed a rapid increase several hours before precipitation, with values exceeding 44 mm/hr,
630 highlighting the accumulation of moisture just before heavy rainfall. These findings align with the
631 notion that increasing atmospheric moisture acts as a precursor to intense precipitation,
632 highlighting the potential of GNSS-based PWV monitoring for tracking moisture and
633 understanding short-term atmospheric fluctuations.

634 The integration of GNSS, infrasound, and seismic data provides a more comprehensive
635 understanding of storm dynamics than any single data source alone. The synergy between these
636 diverse sensor types allows for the detection of atmospheric moisture, lightning activity, rainfall-
637 induced seismic signals, and storm-driven oceanic interactions. Future research should focus on
638 refining unsupervised learning algorithms for infrasound and seismic signal classification,
639 optimizing joint clustering techniques, and improving the integration of these data sources to
640 enhance storm forecasting and early-warning systems. This case study highlights the potential of
641 multi-sensor observations to enhance our understanding of extreme storm behavior and support
642 the development of future early-warning strategies.

643 **6. Conclusions**

644 This study presents a comprehensive analysis of a record-breaking storm over the Black Sea, using
645 a combination of GNSS, infrasound, and seismic data to capture the dynamics of extreme weather
646 events. Our findings underscore the power of multi-sensor networks in enhancing the
647 understanding of storm behavior, particularly in the context of atmospheric moisture, lightning
648 activity, and storm-induced seismic signals. GNSS-derived integrated precipitable water vapor
649 indicates a clear buildup of atmospheric moisture hours before the onset of heavy rainfall,
650 providing valuable insights into the lead-up to extreme precipitation events. Infrasound and
651 seismic data further complemented this analysis, with infrasound providing useful observations of

652 lightning activity and seismic data revealing the link between rainfall intensity and high-frequency
653 seismic noise.

654 The storm analysed here represents an exceptional meteorological event and one of the most
655 intense storms recorded in the region in recent years. According to the ClimaMeter analysis of
656 Antonescu et al. (2024), the characteristics of this storm place it within the broader context of
657 extreme events under changing climate conditions. The integration of GNSS, infrasound, and
658 seismic data provides a more nuanced and holistic view of storm dynamics, highlighting the need
659 for advanced monitoring systems to predict and respond to such extreme events. Looking forward,
660 such multi-sensor approaches may support future developments in integrated environmental
661 monitoring and research into early-warning capabilities, ultimately contributing to improved
662 understanding and characterization of high-impact atmospheric events.

663 **7. Code availability**

664 Seismic data were processed with the open-source python framework for seismology Obspy
665 (Beyreuther et al., 2010). Infrasound data was processed with the WinPMCC software (Le Pichon
666 et al., 2010) developed by CEA/DASE (French Atomic Energy Commission, Environmental
667 Assessment and Monitoring Department) and open-source Python libraries for signal processing.
668 Some of the figures were made with GMT (Generic Mapping Tools, Wessel et al., 2019). The
669 GNSS data was processed using Gamit/Globk (Herring et al., 2020) developed by Massachusetts
670 Institute of Technology (<http://www-gpsg.mit.edu/gg/>).

671 **8. Data availability**

672 Processed infrasound, seismic, and GNSS-derived integrated water vapour data can be visualized
673 and accessed via the INFP monitoring platforms: <https://infp.ro/dashboard-reactive.php> and
674 <https://reactive.infp.ro/events/>. Seismic data are part of the Romanian National Seismic Network
675 maintained by the National institute for Earth Physics (NIEP, www.infp.ro) and are freely
676 available in the miniseed format via EIDA (European Integrated Data Archive,
677 <https://www.orfeus-eu.org/data/eida/>). GNSS data are available for download from NIEP
678 (<http://gps.infp.ro/#/download>) and are provided in the standardized RINEX v2 format, with 24-
679 hour files sampled at 30-second intervals. Infrasound data at AGIR are available to download from
680 NIEP via FDSN dataselect web service. Hourly hydro-meteorological data were obtained from the
681 Copernicus Climate Change Service, Climate Data Store (<https://doi.org/10.24381/cds.bd0915c6>),
682 ERA5 dataset (Hersbach et al., 2023). Limited wind and precipitation data were downloaded from
683 the National Meteorological Agency from <https://www.meteoromania.ro/grafice/> (accessed on
684 13.09.2024) and from https://www.meteoromania.ro/clim/caracterizare-lunara/cc_2024_08.html
685 (accessed on 10.11.2025), respectively. Lightning data came from Meteosat Third Generation
686 Lightning Imager operated by EUMETSAT (The European Organisation for the Exploitation of
687 Meteorological Satellites, <https://www.eumetsat.int/>).

688

689 **9. Author contribution**

690 **Laura Petrescu:** Conceptualization, Methodology, Software, Formal analysis, Data Curation,
691 Writing-Original Draft, Visualization; **Bogdan Antonescu:** Conceptualization, Writing-Review &
692 Editing, Visualization; **Sorin Nistor:** Software, Formal Analysis, Data curation, Visualisation,
693 Writing-Review & Editing; **Iustin Floroiu:** Methodology, Software, Formal analysis, Data
694 Curation, Writing-Original Draft, Visualization; **Dragoş Ene:** Software, Formal analysis, Data
695 Curation, Writing-Review & Editing; **Daniela Ghica:** Software, Formal analysis, Data Curation;
696 **Constantin Ionescu:** Funding Acquisition, Resources, Project administration; **Andrei Anghel:**
697 Methodology, Supervision; **Mihai Dăţcu:** Methodology, Supervision, Funding Acquisition,
698 Resources, Project administration.

699 **10. Acknowledgments**

700 We would like to thank the technicians and staff at NIEP for their support in installing,
701 maintaining, and ensuring the proper functioning of the equipment used in this study. Additionally,
702 we appreciate the efforts of those involved in data formatting and preparation (Cristian Neagoe,
703 Eduard Nastase, Victorin Toader) which were essential for this work. We also thank the two
704 anonymous reviewers for their valuable feedback, which helped improve the manuscript.

705 **11. Financial support**

706 This work was carried out in the framework of the “Competence Center for Climate Change Digital
707 Twin for Earth forecasts and societal redressment” Project PNRR- DTEClimate nr.
708 760008/31.12.2023, subproject Reactive “The Research center for climate change due to natural
709 disasters and extreme weather events”, supported by the Ministry of Research, Innovation and
710 Digitalization of Romania.

711 **12. References**

712 Antonescu, B., Dafis, S., & Faranda, D.: Changes in precipitation patterns driving August 2024
713 Romania floods mostly driven by human-driven climate change. *ClimaMeter, Institut Pierre*
714 *Simon Laplace, CNRS*. <https://doi.org/10.5281/zenodo.14056214>, 2024.

715 Ardhuin, F., Gualtieri, L., Stutzmann, E., Nakata, N. and Fichtner, A.: Physics of ambient noise
716 generation by ocean waves. In *Seismic ambient noise*, Eds: Nakata, N., Gualtieri, L., Fichtner, A.
717 Cambridge University Press, 69-108, <https://doi.org/10.1017/9781108264808.005>, 2019.

718 Assink, J. D., Evers, L. G., Holleman, I., and Paulssen, H.: Characterization of infrasound from
719 lightning, *Geophysical Research Letters*, 35, L15802, <https://doi.org/10.1029/2008GL034193>,
720 2008.

721 Aster, R.C., McNamara, D.E. & Bromirski, P.D.: Multidecadal climate-induced variability in
722 microseisms. *Seismological Research Letters*, 79(2), 194-202,
723 <https://doi.org/10.1785/gssrl.79.2.194>, 2008.

- 724 Aster, R.C., Ringler, A.T., Anthony, R.E., & Lee, T.A.: Increasing ocean wave energy observed
725 in Earth's seismic wavefield since the late 20th century. *Nature Communications*, 14(1), 6984,
726 <https://doi.org/10.1038/s41467-023-42673-w>, 2023.
- 727 Athanase, M., Sánchez-Benítez, A., Monfort, E., Jung, T. and Goessling, H.F.: How climate
728 change intensified storm Boris' extreme rainfall, revealed by near-real-time storylines.
729 *Communications Earth & Environment*, 5(1), 676, <https://doi.org/10.1038/s43247-024-01847-0>,
730 2024.
- 731 Awange, J.L.: Environmental monitoring using GNSS: Global navigation satellite systems,
732 Springer, Heidelberg, <https://doi.org/10.1007/978-3-540-88256-5>, 2012.
- 733 Beyreuther, M., Barsch, R., Krischer, L., Megies, T., Behr, Y. and Wassermann, J.: ObsPy: A
734 Python toolbox for seismology. *Seismological Research Letters*, 81(3), 530-533,
735 <https://doi.org/10.1785/gssrl.81.3.530>, 2010.
- 736 Bengtsson, L., Hodges, K.I. and Roeckner, E.: Storm tracks and climate change. *Journal of*
737 *climate*, 19(15), 3518-3543, <https://doi.org/10.1175/JCLI3815.1>, 2006.
- 738 Bližňák, V. and Sokol, Z.: First validation of the Lightning Imager aboard Meteosat Third
739 Generation satellite with Earth Networks Total Lightning Network. *International Journal of*
740 *Applied Earth Observation and Geoinformation*, 147, 105205,
741 <https://doi.org/10.1016/j.jag.2026.105205>, 2026.
- 742 Bollinger, L., Perrier, F., Avouac, J.P., Sapkota, S., Gautam, U., Tiwari, D.R.: Seasonal
743 modulation of seismicity in the Himalaya of Nepal, *Geophysical Research Letters*, 34(8),
744 <https://doi.org/10.1029/2006GL029192>, 2007.
- 745 Bondár, I., Šindelářová, T., Ghica, D., Mitterbauer, U., Liashchuk, A., Baše, J., Chum, J., Czanik,
746 C., Ionescu, C., Neagoe, C. and Pásztor, M.: Central and Eastern European Infrasound Network:
747 contribution to infrasound monitoring, *Geophysical Journal International*, 230(1), 565-579,
748 <https://doi.org/10.1093/gji/ggac066>, 2022.
- 749 Borzì, A.M., Minio, V., Cannavò, F., Cavallaro, A., D'Amico, S., Gauci, A., De Plaen, R., Lecocq,
750 T., Nardone, G., Orasi, A., Picone, M., Cannata, A.: Monitoring extreme meteo-marine events in
751 the Mediterranean area using the microseism (Medicane Apollo case study). *Scientific Reports*,
752 12(1), <https://doi.org/10.1038/s41598-022-25395-9>, 2022.
- 753 Bosy, J., Kaplon, J., Rohm, W., Sierny, J. and Hadas, T.: Near real-time estimation of water vapour
754 in the troposphere using ground GNSS and the meteorological data, *Annales Geophysicae*, 30,
755 1379–1391, <https://doi.org/10.5194/angeo-30-1379-2012>, 2012.
- 756 Brachet, N., Brown, D., Le Bras, R., Cansi, Y., Mialle, P., Coyne, J.: Monitoring the Earth's
757 Atmosphere with the Global IMS Infrasound Network, in: *Infrasound Monitoring for Atmospheric*

758 Studies, edited by: Le Pichon, A., Blanc, E., Hauchecorne, A. , Springer, Dordrecht,
759 https://doi.org/10.1007/978-1-4020-9508-5_3, 2010.

760 Bromirski, P.D. and Duennebier, F.K.: The near-coastal microseism spectrum: Spatial and
761 temporal wave climate relationships. *Journal of Geophysical Research: Solid Earth*, 107(B8), ESE
762 5-1-ESE 5-20, <https://doi.org/10.1029/2001JB000265>, 2002.

763 Bruyninx, C., Habrich, H., Söhne, W., Kenyeres, A., Stangl, G. and Völksen, C.: Enhancement of
764 the EUREF permanent network services and products, in: Proceedings of the International
765 Association of Geodesy, *Symposium on Geodesy for Planet Earth, Buenos Aires, Argentina, 31*
766 *August-4 September 2009*, 27-34, 2012.

767 Burtin, A., Hovius, N. and Turowski, J.M.: Seismic monitoring of torrential and fluvial processes.
768 *Earth Surface Dynamics*, 4(2), 285-307, <https://doi.org/10.5194/esurf-4-285-2016>, 2016.

769 Butler, R. and Aucan, J.: Multisensor, microseismic observations of a hurricane transit near the
770 ALOHA cabled observatory. *Journal of Geophysical Research: Solid Earth*, 123(4), 3027-3046,
771 2018.

772 Campus, P. and Christie, D.R.: Worldwide observations of infrasonic waves, in: Infrasonic
773 monitoring for atmospheric studies, edited by: Le Pichon, A., Blanc, E., Hauchecorne, A.,
774 Springer, Dordrecht, Netherlands, 185-234, https://doi.org/10.1007/978-1-4020-9508-5_6, 2009.

775 Cansi, Y. and Pichon, A.L.: Infrasonic event detection using the progressive multi-channel
776 correlation algorithm, in: *Handbook of signal processing in acoustics.*, edited by: Havelock, D.,
777 Kuwano, S., Vorländer, M., Springer, New York, 1425-1435, https://doi.org/10.1007/978-0-387-30441-0_77, 2008.

779 Coates, A. and Ng, A.Y.: Learning feature representations with k-means. In *Neural Networks:
780 Tricks of the Trade: Second Edition (561-580)*. Berlin, Heidelberg: Springer Berlin Heidelberg,
781 2012.

782 Coviello, V., Palo, M., Adirosi, E. and Picozzi, M.: Seismic signature of an extreme hydro-
783 meteorological event in Italy, *Natural Hazards*, 1(1), 17, <https://doi.org/10.1038/s44304-024-00018-7>, 2024.

785 Diaz, J., Ruiz, M., Udina, M., Polls, F., Martí, D., Bech, J.: Monitoring storm evolution using a
786 high-density seismic network, *Scientific Reports*, 13(1), <https://doi.org/10.1038/s41598-023-28902-8>, 2023.

788 Díaz, J., Ruiz, M., Sánchez-Pastor, P.S. and Romero, P.: Urban seismology: On the origin of earth
789 vibrations within a city. *Scientific reports*, 7(1), 15296, 2017.

790 Dimitriu, R.G., Stanciu, I.M., Barbu M.-B., Dobrev, N., Dumitru, P.: First results on the western
791 Black Sea coast geodynamics resulted from GeoPontica permanent GNSS stations network data

792 processing, in: Proceedings of the 17th International Multidisciplinary Scientific GeoConference
793 SGEM, Albena, Bulgaria August 2017, 17(11), 149-157, 2017.

794 Dullaart, J.C., Muis, S., Bloemendaal, N. and Aerts, J.C.: Advancing global storm surge modelling
795 using the new ERA5 climate reanalysis. *Climate Dynamics*, 54(1), 1007-1021, 2020.

796 Ebeling, C.W.: Inferring Ocean Storm Characteristics from Ambient Seismic Noise. A Historical
797 Perspective, *Advances in Geophysics*, 53, 1-33. [https://doi.org/10.1016/B978-0-12-380938-](https://doi.org/10.1016/B978-0-12-380938-4.00001-X)
798 4.00001-X, 2012.

799 Enno, S.-E., Viticchie, B., Navia, D. and Grandell, J.: Meteosat-12 Lightning Imager: first year of
800 observations and the main performance characteristics, in: 12th European Conference on Severe
801 Storms, 08 August 2025, <https://doi.org/10.5194/ecss2025-152>, 2025.

802 Faranda, D., Messori, G., Coppola, E., Alberti, T., Vrac, M., Pons, F., Yiou, P., Saint Lu, M., Hisi,
803 A. N. S., Brockmann, P., Dafis, S., Mengaldo, G., and Vautard, R.: ClimaMeter: contextualizing
804 extreme weather in a changing climate, *Weather Climate Dynamics*, 5, 959-983,
805 <https://doi.org/10.5194/wcd-5-959-2024>, 2024.

806 Floroiu, I., Anghel, A., Petrescu, L. and Datcu, M.: Clustering and Feature-Based Similarity
807 Retrieval of Infrasound Events during Two Storms in Constanța, Romania, *International*
808 *Conference on Machine Intelligence for GeoAnalytics and Remote Sensing (MIGARS)*, Bucharest,
809 Romania, 2025, 1-4, <https://doi.org/10.1109/MIGARS67156.2025.11231952>, 2025.

810 Francoeur, J.W., Matoza, R.S., Ortiz, H.D. and De Negri, R.: Identification of transient seismo-
811 acoustic signals from crashing ocean waves: template matching and location of discrete surf
812 events. *Geophysical Journal International*, 243(2), ggaf317, 2025.

813 Garcés, M.A.: On infrasound standards, part 1 time, frequency, and energy scaling. *InfraMatics*,
814 2(2),13–35, <https://doi.org/10.4236/inframatics.2013.22002>, 2013.

815 Gastmeier, W.J. and Howe, B.: Recent studies of infrasound from industrial sources. *Canadian*
816 *Acoustics*, 36(3), 58-59, 2008.

817 Grafkina, M.V., Nyunin, B.N. and Sviridova, E.Y: Environmental monitoring and simulation of
818 infrasound generating mechanism of traffic flow. *Journal of Ecological Engineering*, 20(7),
819 2019.

820 Grevemeyer, I., Herber, R. and Essen, H.H.: Microseismological evidence for a changing wave
821 climate in the northeast Atlantic Ocean. *Nature*, 408(6810), 349-352,
822 <https://doi.org/10.1038/35042558>, 2000.

823 Groos, J.C. and Ritter, J.R.R.: Time domain classification and quantification of seismic noise in
824 an urban environment. *Geophysical Journal International*, 179(2), pp.1213-1231, 2009.

- 825 Gualtieri, L., Camargo, S.J., Pascale, S., Pons, F.M.E., & Ekström, G.: The persistent signature of
826 tropical cyclones in ambient seismic noise, *Earth and Planetary Science Letters*, 484, 287-294.
827 <https://doi.org/10.1016/j.epsl.2017.12.026>, 2018.
- 828 Guerova, G., Jones, J., Douša, J., Dick, G., de Haan, S., Pottiaux, E., Bock, O., Pacione, R.,
829 Elgered, G., Vedel, H. and Bender, M.: Review of the state of the art and future prospects of the
830 ground-based GNSS meteorology in Europe, *Atmospheric Measurement Techniques*, 9(11),
831 5385–5406, <https://doi.org/10.5194/amt-9-5385-2016>, 2016.
- 832 Herring, T., King, R., Floyd, M., McClusky, S.: GAMIT Reference Manual GPS Analysis at MIT
833 Release 10.7. GAMIT/GLOBK, 2020.
- 834 Hersbach, H., Bell, B., Berrisford, P., Hirahara, S., Horányi, A., Muñoz-Sabater, J., Nicolas, J.,
835 Peubey, C., Radu, R., Schepers, D. and Simmons, A.: The ERA5 global reanalysis, *Quarterly*
836 *Journal of the Royal Meteorological Society*, 146(730), 1999-2049, 2020.
- 837 Hersbach, H., Bell, B., Berrisford, P., Biavati, G., Horányi, A., Muñoz Sabater, J., Nicolas, J.,
838 Peubey, C., Radu, R., Rozum, I., Schepers, D., Simmons, A., Soci, C., Dee, D., Thépaut, J-N.:
839 ERA5 hourly data on single levels from 1940 to present. Copernicus Climate Change Service
840 (C3S) Climate Data Store (CDS), <https://doi.org/10.24381/cds.adbb2d47>, 2023.
- 841 Holmlund, K., Grandell, J., Schmetz, J., Stuhlmann, R., Bojkov, B., Munro, R., Lekouara, M.,
842 Coppens, D., Viticchie, B., August, T. and Theodore, B.: Meteosat Third Generation (MTG):
843 Continuation and innovation of observations from geostationary orbit, *Bulletin of the American*
844 *Meteorological Society*, 102(5), E990-E1015, <https://doi.org/10.1175/BAMS-D-19-0304.1>, 2021.
- 845 Hua, J., Wu, M., Mulholland, J.P., Neelin, J.D., Tsai, V.C. and Trugman, D.T.: High-resolution
846 precipitation monitoring with a dense seismic nodal array. *Scientific Reports*, 13(1), 11450,
847 <https://doi.org/10.1038/s41598-023-38008-w>, 2023.
- 848 Hupe, P., Ceranna, L., Pilger, C., de Carlo, M., Le Pichon, A., Kaifler, B. and Rapp, M.: Assessing
849 middle atmosphere weather models using infrasound detections from microbaroms. *Geophysical*
850 *Journal International*, 216(3), 1761-1767, <https://doi.org/10.1093/gji/ggy520>, 2019.
- 851 Hupe, P., Ceranna, L., Le Pichon, A., Matoza, R.S. and Mialle, P.: International Monitoring
852 System infrasound data products for atmospheric studies and civilian applications. *Earth System*
853 *Science Data Discussions*, 14, 4201–4230, <https://doi.org/10.5194/essd-14-4201-2022>, 2022.
- 854 Iliescu, A. I., Rus, T., Danciu, V., Moldoveanu, C., & Ilie, A.: Current situation of GNSS networks
855 in Romania, *Bulletin of University of Agricultural Sciences and Veterinary Medicine Cluj-Napoca.*
856 *Horticulture*, 76(2), 2019.
- 857 Jakobsen, J.: Infrasound emission from wind turbines. *Journal of low frequency noise, vibration*
858 *and active control*, 24(3), 145-155, 2005.

859 Jiao, D., Xu, N., Yang, F. and Xu, K.: Evaluation of spatial-temporal variation performance of
860 ERA5 precipitation data in China. *Scientific Reports*, 11(1), 17956, 2021.

861 Johnston, G., Riddell, A. and Hausler, G.: The international GNSS service, in: Springer handbook
862 of global navigation satellite systems, edited by: Teunissen, P.J. and Montenbruck, O., Springer,
863 Cham, Switzerland, 967-982, https://doi.org/10.1007/978-3-319-42928-1_33, 2017.

864 Jones, J., Guerova, G., Douša, J., Dick, G., de Haan, S., Pottiaux, E., Bock, O., Pacione, R. and
865 Van Malderen, R.: Advanced GNSS tropospheric products for monitoring severe weather events
866 and climate, COST Action ES1206 Final Action Dissemination Report, 563, 2020.

867 Karabatić, A., Weber, R. and Haiden, T.: Near real-time estimation of tropospheric water vapour
868 content from ground based GNSS data and its potential contribution to weather now-casting in
869 Austria, *Advances in Space Research*, 47(10), 1691–1703,
870 <https://doi.org/10.1016/j.asr.2010.10.028>, 2011.

871 Kober, K. and Tafferner, A.: Tracking and nowcasting of convective cells using remote sensing
872 data from radar and satellite, *Meteorologische Zeitschrift*, 1(18), 75-84,
873 <https://doi.org/10.1127/0941-2948/2009/359>, 2009.

874 Koper, K.D. & Burlacu, R.: The fine structure of double-frequency microseisms recorded by
875 seismometers in North America. *Journal of Geophysical Research: Solid Earth*, 120(3), 1677-
876 1691. <https://doi.org/10.1002/2014JB011820>, 2015.

877 Kokou, P.: Status of the MTG-II Lightning Imager commissioning activities, in: EUMETSAT
878 Conference 2023, 1-C GEO – MTG, Malmö, Sweden, 12 September 2023, 2023.

879 Landès, M., Ceranna, L., Le Pichon, A. and Matoza, R.S.: Localization of microbarom sources
880 using the IMS infrasound network. *Journal of Geophysical Research: Atmospheres*, 117(D6),
881 <https://doi.org/10.1029/2011JD016684>, 2012.

882 Landskron, D., Böhm, J.: VMF3/GPT3: refined discrete and empirical troposphere mapping
883 functions, *Journal of Geodesy*, 92, 349–360, <https://doi.org/10.1007/s00190-017-1066-2>, 2018.

884 Li, L., Boué, P., Retailleau, L., & Campillo, M.: Spatiotemporal Correlation Analysis of Noise-
885 Derived Seismic Body Waves With Ocean Wave Climate and Microseism Sources, *Geochemistry,*
886 *Geophysics, Geosystems*, 21(9), <https://doi.org/10.1029/2020GC009112>, 2020.

887 Listowski, C., Forestier, E., Dafis, S., Farges, T., De Carlo, M., Grimaldi, F., Le Pichon, A.,
888 Vergoz, J., Heinrich, P. and Claud, C.: Remote monitoring of Mediterranean hurricanes using
889 infrasound, *Remote Sensing*, 14(23), 6162, <https://doi.org/10.3390/rs14236162>, 2022.

890 MacQueen, J.: Some methods for classification and analysis of multivariate observations, in:
891 Proceedings of the Fifth Berkeley Symposium on Mathematical Statistics and Probability,
892 Berkeley, California, January 1967, 5, 281-298, 1967.

893 Marut, G., Hadas, T., Kaplon, J., Trzcina, E. and Rohm, W.: Monitoring the water vapor content
894 at high spatio-temporal resolution using a network of low-cost multi-GNSS receivers, *IEEE*
895 *Transactions on Geoscience and Remote Sensing*, 60, 1-14,
896 <https://doi.org/10.1109/TGRS.2022.3226631>, 2022.

897 Nistor, S., Suba, N.S., Maciuk, K., Kudrys, J., Nastase, E.I. and Muntean, A.: Analysis of noise
898 and velocity in GNSS EPN-repro 2 time series, *Remote Sensing*, 13(14), 2783,
899 <https://doi.org/10.3390/rs13142783>, 2021a.

900 Nistor, S., Suba, N.S., El-Mowafy, A., Apollo, M., Malkin, Z., Nastase, E.I., Kudrys, J. and
901 Maciuk, K.: Implication between geophysical events and the variation of seasonal signal
902 determined in GNSS position time series, *Remote Sensing*, 13(17), 3478,
903 <https://doi.org/10.3390/rs13173478>, 2021b.

904 Pásztor, M., Czanik, C. and Bondár, I.: A single array approach for infrasound signal
905 discrimination from quarry blasts via machine learning, *Remote Sensing*, 15(6), 1657,
906 <https://doi.org/10.3390/rs15061657>, 2023.

907 Le Pichon, A., Matoza, R., Brachet, N. and Cansi, Y.: Recent enhancements of the PMCC
908 infrasound signal detector. *Inframatrics*, 26, 5-8, 2010.

909 Price, I., Sanchez-Gonzalez, A., Alet, F., Andersson, T.R., El-Kadi, A., Masters, D., Ewalds, T.,
910 Stott, J., Mohamed, S., Battaglia, P. and Lam, R.: Probabilistic weather forecasting with machine
911 learning. *Nature*, 637(8044), 84-90, 2025

912 Priego, E., Jones, J., Porres, M.J. and Seco, A.: Monitoring water vapour with GNSS during a
913 heavy rainfall event in the Spanish Mediterranean area, *Geomatics, Natural Hazards and Risk*,
914 8(2), 282–294, <https://doi.org/10.1080/19475705.2016.1201150>, 2017.

915 Retailleau, L. & Gualtieri, L.: Multi-phase seismic source imprint of tropical cyclones, *Nature*
916 *Communications*, 12(1), <https://doi.org/10.1038/s41467-021-22231-y>, 2021.

917 Rindraharisaona, E.J., Réchou, A., Fontaine, F.R., Barruol, G., Stamenoff, P., Boudevillain, B.,
918 Rigaud-Louise, F. and Delcher, E.: Seismic signature of rain and wind inferred from seismic data,
919 *Earth and Space Science*, 9(10), p.e2022EA002328, 2022.

920 Šindelářová, J., Chum, J., Skripnikova, K., and Base, J.: Atmospheric infrasound observed during
921 intense convective storms on 9–10 July 2011, *Journal of Atmospheric and Solar-Terrestrial*
922 *Physics*, 122, 66–74, <https://doi.org/10.1016/j.jastp.2014.10.014>, 2015.

923 Šindelářová, T., De Carlo, M., Czanik, C., Ghica, D., Kozubek, M., Podolská, K., Baše, J., Chum,
924 J., and Mitterbauer, U.: Infrasound signature of the post-tropical storm Ophelia at the Central and
925 Eastern European Infrasound Network, *Journal of Atmospheric and Solar-Terrestrial Physics*, 217,
926 105603, <https://doi.org/10.1016/j.jastp.2021.105603>, 2021.

- 927 Smirnov, A., De Carlo, M., Le Pichon, A., Shapiro, N.M. and Kulichkov, S.: Characterizing the
928 oceanic ambient noise as recorded by the dense seismo-acoustic Kazakh network. *Solid Earth*,
929 *12*(2), 503-520, 2021.
- 930 Soci, C., Hersbach, H., Simmons, A., Poli, P., Bell, B., Berrisford, P., Horányi, A., Muñoz-Sabater,
931 J., Nicolas, J., Radu, R. and Schepers: The ERA5 global reanalysis from 1940 to 2022. *Quarterly*
932 *Journal of the Royal Meteorological Society*, *150*(764), 4014-4048, 2024.
- 933 Sokol, Z., Szturc, J., Orellana-Alvear, J., Popova, J., Jurczyk, A. and Céleri, R.: The role of
934 weather radar in rainfall estimation and its application in meteorological and hydrological
935 modelling—A review, *Remote Sensing*, *13*(3), 351, 2021.
- 936 Stopa, J.E., Cheung, K.F., Garcés, M.A. and Badger, N.: Atmospheric infrasound from nonlinear
937 wave interactions during Hurricanes Felicia and Neki of 2009, *Journal of Geophysical Research:*
938 *Oceans*, *117*(C12), <https://doi.org/10.1029/2012JC008257>, 2012
- 939 Stott, P.: How climate change affects extreme weather events. *Science*, *352*(6293), 1517-1518,
940 <https://doi.org/10.1126/science.aaf7271>, 2016.
- 941 Tanimoto, T. & Anderson, A.: Seismic noise between 0.003 Hz and 1.0 Hz and its classification,
942 *Progress in Earth and Planetary Science*, *10*(1), <https://doi.org/10.1186/s40645-023-00587-7>,
943 2023.
- 944 Taweessintananon, K., Landrø, M., Potter, J.R., Johansen, S.E., Rørstadbotnen, R.A., Bouffaut, L.,
945 Kriesell, H.J., Brenne, J.K., Haukanes, A., Schjelderup, O. and Storvik, F.: Distributed acoustic
946 sensing of ocean-bottom seismo-acoustics and distant storms: A case study from Svalbard,
947 Norway. *Geophysics*, *88*(3), B135-B150, 2023.
- 948 Tiberia, A., Mascitelli, A., D'adderio, L.P., Federico, S., Marisaldi, M., Porcù, F., Realini, E.,
949 Gatti, A., Ursi, A., Fuschino, F. and Tavani, M.: Time evolution of storms producing terrestrial
950 gamma-ray flashes using ERA5 reanalysis data, GPS, lightning and geostationary satellite
951 observations. *Remote Sensing*, *13*(4), 784, 2021.
- 952 Vaquero-Martínez, J. and Antón, M.: Review on the role of GNSS meteorology in monitoring
953 water vapor for atmospheric physics, *Remote Sensing*, *13*(12), 2287,
954 <https://doi.org/10.3390/rs13122287>, 2021.
- 955 Viticchie, B., Lekouara, M., Hungershofer, K., Joro, S., Grandell, J., Maufrais, A., Marquez, M.J.,
956 Munro, R.: Algorithm Theoretical Basis Document (ATBD) for L2 processing of the MTG
957 Lightning Imager data, Rapp. Tech. EUMESTAT, 6, 2020.
- 958 Waxler, R., Frazier, W. G., Talmadge, C. L., Liang, B., Hetzer, C., Buchanan, H., and Audette, W.
959 E.: Analysis of infrasound array data from tornadic storms in the southeastern United States,
960 *Journal of the Acoustical Society of America*, *156*, 1903–1919,
961 <https://doi.org/10.1121/10.0028815>, 2024.

962 Wessel, P., Luis, J.F., Uieda, L.A., Scharroo, R., Wobbe, F., Smith, W.H. and Tian, D.: The generic
963 mapping tools version 6, *Geochemistry, Geophysics, Geosystems*, 20(11), 5556-5564,
964 <https://doi.org/10.1029/2019GC008515>, 2019.

965 Wilgan, K., Rohm, W. and Bosy, J.: Multi-observation meteorological and GNSS data comparison
966 with numerical weather prediction model, *Atmospheric Research*, 156, 29–42,
967 <https://doi.org/10.1016/j.atmosres.2014.12.011>, 2015.

968 Wu, G., Qin, S., Mao, Y., Ma, Z. and Shi, C.: Validation of precipitation events in ERA5 to gauge
969 observations during warm seasons over eastern China. *Journal of Hydrometeorology*, 23(5), 807-
970 822, 2022.

971